Projectile Combustion Effects on Ram Accelerator Performance

Saarth Anjali Chitale

A thesis

submitted in partial fulfillment of the

requirement for the degree of

Master of Science in Aeronautics and Astronautics

University of Washington

2016

Committee:

Carl Knowlen

Mitsuru Kurosaka

Program Authorized to Offer degree:

Aeronautics and Astronautics

University of Washington

Abstract

Projectile Combustion Effects on Ram Accelerator Performance

Saarth Anjali Chitale

Chair of the Supervisory Committee:

Prof. Carl Knowlen

William E. Boeing Department of Aeronautics and Astronautics

The ram accelerator facility at the University of Washington is used to propel projectiles at supersonic velocities. This concept is similar to an air-breathing ramjet engine in that sub-caliber projectiles, shaped like the ramjet engine center-body, are shot through smooth-bore steel-walled tubes having an internal diameter of 38 mm. The ram accelerator propulsive cycles operate between Mach 2 to 10 and have the potential to accelerate projectile to velocities greater than 8 km/s. The theoretical thrust versus Mach number characteristics can be obtained using knowledge of gas dynamics and thermodynamics that goes into the design of the ram accelerator. The corresponding velocity versus distance profiles obtained from the test runs at the University of Washington, however, are often not consistent with the theoretical predictions after the projectiles reach in-tube Mach numbers greater than 4. The experimental velocities are typically greater than the expected theoretical predictions; which has led to the proposition that the combustion process may be moving up onto the projectile.

An alternative explanation for higher than predicted thrust, which is explored here, is that the performance differences can be attributed to the ablation of the projectile body which results in molten metal being added to the flow of the gaseous combustible mixture around the projectile. This molten metal is assumed to mix uniformly and react with the gaseous propellant; thereby enhancing the propellant energy release and altering the predicted thrust-Mach characteristics. This theory predicts at what Mach number the projectile will first experience enhanced thrust and the corresponding velocity-distance profile. Preliminary results are in good agreement with projectiles operating in methane/oxygen/nitrogen propellants. Effects of projectile surface to volume ratio are

also explored by applying the model to experimental results from smaller (Tohoku University, 25-mm-bore) and larger (Institute of Saint-Louis 90-mm-bore) bore ram accelerators. Due to lower surface-to-volume ratio, large diameter projectiles are predicted to need to reach higher Mach numbers than smaller diameter projectiles before thrust enhancement due to metal ablation and burning would be experienced. This proposition was supported by published experimental data. The theoretical modeling of projectile ablation, metal combustion, and subsequent ram accelerator thrust characteristics are presented along comparisons to experiments from three different sized ram accelerator facilities.

Table of Contents

LIST OF TABLES

List of Figures

Nomenclature

A	tube cross-sectional area
c_p	constant pressure specific heat capacity
F	thrust
h	static enthalpy
h_f	enthalpy of formation at 0 degree Kelvin
I	non-dimensional thrust coefficient (defined as F/p_1A)
M	Mach number
m_p	projectile mass
p_1	fill pressure
p	static pressure
p_t	total pressure
Q	non-dimensional heat parameter (defined as $\Delta h_f/c_pT$)
S	entropy
T	static temperature
U	projectile velocity
γ	specific heat ratio
Δq	heat of reaction of the propellant gas mixtures
$\frac{\partial T}{\partial y}$	temperature gradient in the 'y' direction
T_m	melting temperature of the projectile material
V_a	ablation velocity
ξ	variable corresponding to 'y'

Acknowledgement

I would like to express my deepest gratitude for my advisor, Dr. Carl Knowlen, who has been a tremendous help at every point in the completion of this thesis. I have learnt much more than academic skills from him, the most important of which would be patience and perseverance. I would also like to thank him for extensively editing and refining my thesis.

I would also like to thank all the Master's and Doctoral students who worked relentlessly on the ram accelerator to create all the data for me to use and analyze.

Things were made much easy on ANSYS and MATLAB due to my friends Aditya Dandekar, University of Texas and Ward Handley, University of Washington, Seattle. I would like to thank both of them from the bottom of my heart for all their help and support.

Last but not the least I would like to thank the lovely Swarada Yadav, who has supported me tremendously in every way she could when I needed her the most.

This thesis is dedicated to the memory of my mother, Anjali Chitale.

She has been my pillar of strength

She inspires me to be dedicated and hard-working and to dream Big!

Chapter 1 Introduction

The ram accelerator is a device for propelling projectiles to very high velocities starting from some finite initial velocity in a way similar to that of a conventional ramjet engine (1). The projectile shape is that of a ramjet engine center-body, which is used to diffuse the incoming supersonic flow to subsonic values, with a stationary metal tube in the place of the ramjet engine's outer cowling as shown in Fig. 1.1 (2).

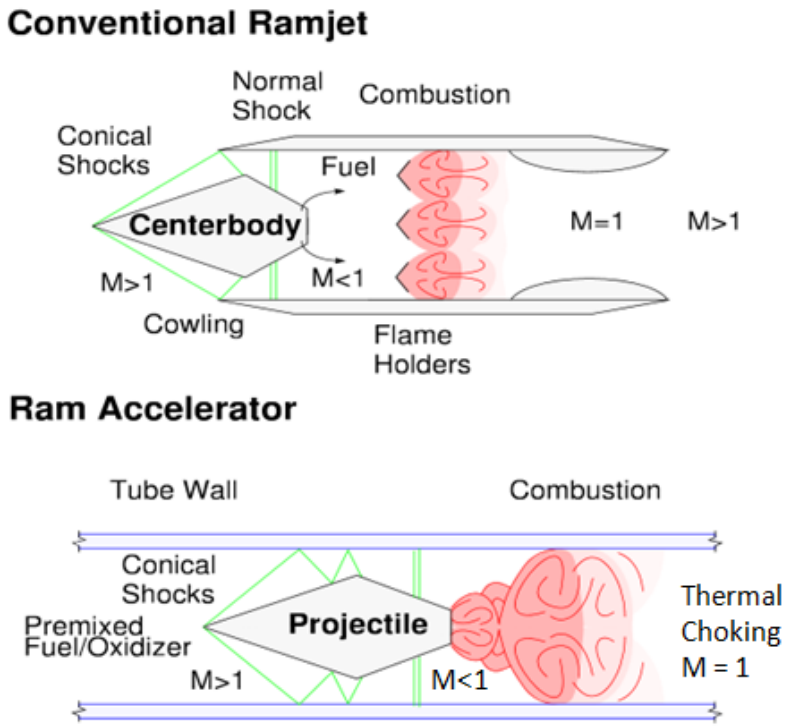

Fig. 1.1 Conventional Ramjet and thermally choked ram accelerator

The projectile in injected into the ram accelerator tube at supersonic entrance velocity with a light gas gun (3). Upon entrance to the ram accelerator, combustion is initiated behind the projectile, producing a wave-like pressure pulse which travels with the projectile (3). The projectile 'surfs' on this wave of high pressure gas. As opposed to a conventional gun in which the highest pressure is always in the beginning of the breech, the highest pressure gas travels with the projectile thus providing high values of acceleration and greater ballistic efficiency (4). Ballistic efficiency is defined here as the ratio of the rate of change of kinetic energy to the rate of chemical energy release.

Out of the several modes of ram accelerator propulsion, which are classified according to the velocity of the projectile relative to the Chapman-Jouguet (C-J) detonation velocity of the mixture, V_{CJ} (5), only the thermally choked mode will be considered in this thesis. When the projectile velocity is less than ~90% V_{CJ}, the ram accelerator is assumed to operate in the thermally choked propulsive mode. In this mode, a shock system stabilizes on the projectile and compresses the flow thus raising the pressure and temperatures drastically. In the reference frame of the projectile, the oncoming gas is

slowed down to subsonic speeds before it encounters a zone of combustion at the base of the projectile as shown in Fig. 1.1. The combustion raises the temperature which in turn causes the flow to choke thermally at some point behind the projectile. The resulting flow creates a pressure distribution about the projectile which results in a positive thrust which accelerates the projectile to very high Mach numbers. In the thermally choked mode, the normal shock recedes on the body and the thrust decreases as the velocity of the projectile increases. Theoretically, the normal shock falls off the body and the thrust approaches zero as the projectile velocity approaches the C-J velocity. However, experimentally is has been shown that the projectile accelerates smoothly through the C-J velocity of the propellant mixtures (5).

Theoretical predictions of the thrust versus Mach characteristics for any particular propellant mixture can be obtained from the ram accelerator Hugoniot (4) in terms of a non-dimensional thrust coefficient, $I = F/p_1A$. However, the non-dimensional thrust coefficients obtained experimentally have shown some differences from the theoretical predictions and this phenomenon is hypothesized to occur due to the melting and subsequent combustion of the projectile metal body (6), (7). Efforts were made previously to model the ablation of the nose cone (8). However, ablation of the nose cone was not considered to contribute in the combustion process to account for the offset between experiments and the theory. Thus, to model the ablation of the projectile material and its subsequent combustion to predict the experimental non-dimensional thrust coefficient versus Mach profile is the focus of this thesis.

Chapter 2 Theoretical Investigation

In this chapter, the theory for developing the one dimensional thrust versus Mach profile relation, the ablation model and the assumptions made for simplifying the modeling process (modeling the ablation into the velocity-distance profile) are discussed in detail.

2.1 Ram Accelerator Hugoniot

Analysis of the thermodynamics of the general ram accelerator process proceeds in a similar manner to that used for conventional one dimensional shock and detonation waves (9)- (10). The conservation equations of gas dynamics are applied across the control volume shown in Fig. 2.1 (4). It consists of the entrance boundary, exit boundary and the side walls to which an arbitrary body is attached. The gaseous propellant mixture, both before and after combustion, is assumed to behave as an ideal gas with temperature dependent heat capacities. Jump conditions across the control volume for the mass, energy and momentum conservation equations are:

$$\frac{u_1}{v_1} = \frac{u_6}{v_6} \tag{2.1.1}$$

$$h_1 + \frac{u_1^2}{2} + h_{f1} = h_6 + \frac{u_6^2}{2} + h_{f6} \tag{2.1.2}$$

$$p_1 + \frac{u_1^2}{v_1} + \frac{F}{A} = p_6 + \frac{u_6^2}{v_6} \tag{2.1.3}$$

Here, v is the specific volume of the propellant mixture, u is the flow velocity, h is the static enthalpy, h_f is the enthalpy of formation for the gas mixture (at zero degrees Kelvin), p is the static pressure, A is the cross sectional area of the tube and F is the axial force exerted on the flow by the body within the control volume. Subscripts 1 and 6 refer to entrance and exit properties of the propellant mixture, respectively.

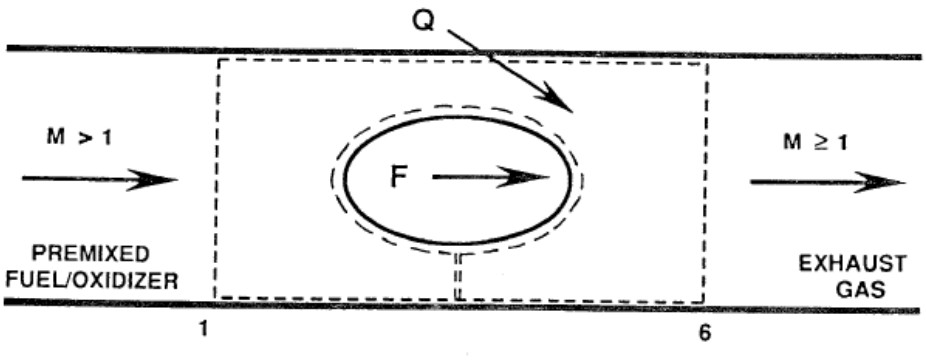

Fig. 2.1 Control volume for analysis of general ram accelerator propulsion cycle

Final states '6' of the flow allowable from any initial state '1' in the pressure-specific volume plane are determined from this system of equations for any steady flow process that occurs within the straight-walled tube. This includes processes involving chemical reactions that occur in a region of reduced flow area, somewhere within the control volume, which results in a change in the momentum flux when the flow is brought back to the original flow area.

Initial and final flow velocities may be written in terms of a non-dimensional 'thrust coefficient'- defined as $I = \frac{F}{p_1 A_1}$ and the initial and final propellant gas pressures and specific volume by combining the mass and momentum equations to yield the following:

$$u_1^2 = v_1^2 \left[\frac{p_6 - p_1(I+1)}{v_1 - v_6}\right] \tag{2.1.4}$$

$$u_6^2 = v_6^2 \left[\frac{p_6 - p_1(I+1)}{v_1 - v_6}\right] \tag{2.1.5}$$

Considering the above equations and the definition of the non-dimensional thrust coefficient and Mach number, the following equation is obtained (1):

$$I = \frac{F}{p_1 A_1} = \frac{p_6}{p_1}(1 + \gamma_6) - (1 + \gamma_1 M_1^2) \tag{2.1.6}$$

where, γ_1 & γ_6 are the specific heat ratios before and after combustion, respectively, which is assumed to be terminated by thermal choking at the exit plane; i.e. $M_6 = 1$.

From continuity and ideal gas laws, the following relation can be obtained:

$$\frac{p_6}{p_1} = M_1 \left[\left(\frac{T_6}{T_1}\right)\left(\frac{\gamma_1 m_1}{\gamma_6 m_6}\right)\right]^{1/2} \tag{2.1.7}$$

Where, T_1 & T_6 are the static temperatures and m_1 & m_6 are the molecular weights before after combustion, respectively.

Using the isentropic relations at stations '1' and '6', the temperature ratio can be expressed as follows:

$$\frac{T_6}{T_1} = \frac{T_{t6}}{T_{t1}}\left[\frac{2 + (\gamma_1 - 1)M_1^2}{\gamma_6 + 1}\right] \tag{2.1.8}$$

where, the subscript 't' denotes stagnation conditions.

The stagnation temperature ratio is obtained from application of the energy equation across the control volume as follows:

$$\frac{T_{t6}}{T_{t1}} = \frac{C_{p1}}{C_{p6}}\left(1 + \frac{\Delta q}{C_{p1} T_1}\right) \tag{2.1.9}$$

Here, C_{p1} and C_{p2} are the specific heats at constant pressure before and after combustion, respectively. The parameter Δq is the heat of reaction of the propellant gas mixtures.

Substituting equations (2.1.7)-(2.1.9) into equation (2.1.6) yields:

$$I = \frac{F}{p_1 A_1} = \frac{\gamma_1 M_1}{\gamma_6}\left\{2\left(\frac{\gamma_6^2 - 1}{\gamma_1 - 1}\right)\left[1 + \frac{\gamma_1 - 1}{2}M_1^2 + \frac{\Delta q}{C_{p1} T_1}\right]\right\}^{\frac{1}{2}} - (1 + \gamma_1 M_1^2) \tag{2.1.10}$$

It can be seen that the thrust is directly proportional to the initial propellant fill pressure, p_1.

Considering equation (3.10) with Newton's second law of motion, we have the following:

$$\frac{dU_1}{dx} = \frac{F}{mU_1} = \frac{I}{mU_1} PA \tag{2.1.11}$$

Numerically integrating the above equation with MATLAB gives the velocity-distance profile from the non-dimensional thrust coefficient as described in step 8 in the upcoming chapter on Modeling Procedure for the metal ablation modeling.

2.2 Ablation Model

Ablation is defined as the loss of material due to melting and subsequent removal due to exposure to high speed flows (11). It is different from erosion in the sense that the material is primarily lost due to melting as opposed to abrasion or friction acting on the surface of the metal due to low or high speed flows.

The solid wall of the projectile is exposed to a high heat flux as it accelerates through the propellant mixture. This heat flux results from convection from the high temperature, high speed boundary layer. As a result of the high heat flux the solid body melts and a portion of the surface is removed (12). If this process is essentially one dimensional, the appropriate differential equation can be written as:

$$\frac{\partial T}{\partial y} = \frac{1}{\alpha}\frac{\partial T}{\partial \tau} \tag{2.2.1}$$

Here we consider the co-ordinate system is set in such a way that *y* is perpendicular to the surface and *x* is parallel to it.

Solving this equation and evaluating all constants the final solution to the above equation is

$$\frac{T-T_i}{T_m-T_i} = \exp\left(-\frac{V_a \xi}{\alpha}\right) \tag{2.2.2}$$

In the above equation, $\xi = y - V_a\tau$, T_i is the initial temperature, T_m is the melting temperature and V_a is the ablation velocity (12),

$$V_a = \frac{\dot{q}}{\rho H_{ab}\left[1+{}^{c(T_m-T_i)}/_{H_{ab}}\right]} \tag{2.2.3}$$

Here, *c* is the heat transfer coefficient and H_{ab}, the heat of ablation.

The total energy incident on the body is either conducted into the body or used to melt the material. Thus,

$$\dot{q}_{tot} = \dot{q}_{cond} + \dot{q}_{abl} \tag{2.2.4}$$

Heat of ablation can be thought of as the heat of melting of the solid projectile material (7).

The ratio for the heat which is conducted into the solid and the total heat incident on the projectile is given by the following equation (12):

$$\frac{Q_{cond}}{Q_{total}} = \frac{c(T_m - T_i)}{H_{ab}\left[1 + {}^{c(T_m - T_i)}/_{H_{ab}}\right]} \tag{2.2.5}$$

The numerical method to compute this division of heat between the heat of ablation and heat of melting (13) will not be considered in this thesis. Instead the heat of melting will be taken into account on ANSYS Transient thermal module (14).

2.3 Assumptions

An analytical model was developed which determined the rate of metal ablation as a function of velocity and time-of-flight of the projectile while operating in the thermally choked ram accelerator propulsive mode. The molten metal (Mg or Al) was added to the gaseous propellant mixture flow and the chemical equilibrium under thermal choking conditions were determined. The resultant thrust acting on the projectile as function of Mach number was then used to predict velocity-distance profiles for comparison with experiment. The details of the modeling assumptions for ablation, thermo-chemistry calculations, and thrust predictions are presented here.

2.3.1 Projectile Geometry and Aerodynamics

The actual projectiles typically have a conical nose followed by the frustum of a cone which tapers down to a bluff base, as shown in Fig. 2.2. The nose cone angles vary from 7 to 20 degree half angles and their base diameters are typically about 76% of the tube diameter, forming a ‘throat’ with a flow area contraction ratio of 42%. The aft-body taper angle ranges from 2 to 5 degrees, body length is typically 1.8 to2.5 times the tube diameter, and the base diameter is typically 47 to 50% of the tube diameter. Fins are used to center the projectile in the tube and can number from 3 to 6. Fin leading edges are usually raked back at angles ranging from 10 to 45 degrees, and their leading edges can be blunt or knife-edged. For ablation modeling purposes, the projectile geometry is simplified while preserving the main geometric features as iterated in the following list of assumptions.

The projectile body is a perfect cylinder with the fins being rectangular in shape and covering the entire span of the projectile cylindrical body length.

1. This assumption simplifies the analysis made using ANSYS as well as designing the geometry and related mesh.

The shock system comprising of oblique shocks on the nose cone of the projectile are ignored because their influence on heat transfer has been shown to be negligible for the Mach number range and time-of-flight experienced by thermally choked ram accelerated projectiles (8), (13). It is assumed that normal shock is situated at the throat of the projectile which renders the flow subsonic over the

projectile cylindrical body. The aero-thermodynamic heating of the projectile body is then determined from subsonic flow conditions where the total temperature corresponds to that of the projectile's in-tube Mach number.

2. This assumption eliminates the need to calculate the temperature and pressure variations across every oblique and normal shock wave produced along the projectile body.

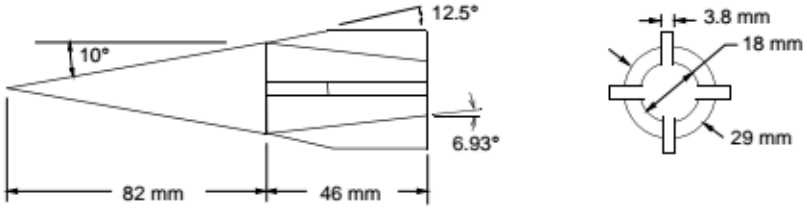

Fig. 2.2 Actual projectile details for 38-mm-bore ram accelerator

2.3.2 Mixture Chemistry

The actual propellant mixture chemistries used for each ram shot may vary; the amount of oxygen can range from 2-3 moles, the range for methane is 2-6 moles while nitrogen can vary from 5-12 moles. For ablation modeling purposes, the following assumptions make it possible to analyze multiple experimental data sets considering particular propellant mixture chemistry.

The propellant mixture chemistries with and without the addition of metal fuel are considered to have comparable properties, and thus similar thrust characteristics, if their detonation velocities are within 5%.

1. If the difference between these detonation velocities is small as noted in the assumption then the thrust profile does not vary.

The non dimensional thrust versus Mach profile obtained for a particular fill pressure and chemistry can be used to obtain the velocity-distance profile at any fill pressure.

2. This assumption implies that real gas effects are not significant for the conditions being considered here, which is generally true for fill pressures less than 3 MPa (15), (16).

2.3.3 Ablation Modeling

The three dimensional heat conduction into the projectile body was approximated by calculating the convective heat transfer into a straight, thin-walled cylinder for the aftbody and rectangular plates for the fins. The potential for only a portion of the ablated metal to be converted to gaseous phase was considered. Conversely, the influence on total temperature and pressure around the cylindrical body of the projectile due to the combustion of the ablated metal and the propellant mixture in the ram tube was not included in the modeling.

The heat transfer is one dimensional i.e. the heat transfer parallel to the projectile body is ignored.

1. The relatively thin walled geometry of the cylindrical body and flat fins allow very little axial heat conduction in the time scale of the experiments, thus these effects were neglected in this analysis.

The amount of molten metal in liquid state which does not change phase to gaseous state at each time step is not taken into account for the next time step calculations of thrust.

2. Since the calculation for the heat transfer coefficient at each time step is based on the chemical mixture, including the amount of molten metal from the previous time step will increase the complexity of the calculations while not changing the results significantly.

The effects of temperature and pressure rise due to combustion of the metal at each time step is ignored when considering the condition for the calculation of combustion/detonation parameter in the next time step.

3. The model developed in this thesis focuses mainly on the effects of aerodynamic heating on ablation and the subsequent increase in the thrust obtained. The potential coupling of enhanced heating due to metal combustion with the ablation model is not considered.

2.4 Ablation Modeling Procedure

The predicted molten metal mass flux arising from ablation is determined using ANSYS and the corresponding thrust-Mach and the velocity-distance profiles for various bore diameters are subsequently obtained. To develop this model, the acceleration of the projectile is assumed to be 10^5 m/s^2 with the initial velocity of the projectile considered to be 1000 m/s. The experimental results used in this thesis have acceleration values and initial velocities somewhat close to those assumed in the ablation model. The flow properties including aerodynamic heating, molar flow rates of the chemical mixture, viscosities and ratio of specific heats are computed up to Mach number of 5. To compute this, time steps of 0.5 ms are considered since resolution lower than this does not produce a significant difference in the thrust and velocity-distance profiles. Thus, acceleration, initial velocity of the projectile and the time step form the basis to compute various flow parameters, the velocity, Mach number and the rate of molten metal addition at these corresponding Mach numbers.

Numerous steps are involved in obtaining the required thrust-Mach number and velocity-distance profiles based on the assumed average acceleration and initial projectile velocity. A detailed discussion of these steps is presented in the following sections, for a representative case of an aluminum projectile in a 38-mm-bore ram accelerator experiment.

2.4.1 Step 1

The flow rate of the chemical mixture inside the ram tube is calculated using the fill pressure, area of the tube and the velocity of the projectile at each time step. This is needed so that the correct mole ratio of metal addition can be used in thermo-chemical calculations as function of Mach number.

For the sample case considered, the chemical mixture in the tube is $2.7CH_4 + 2O_2 + 5.8N_2$. Here, the fuel is methane, oxygen is the oxidizer while the diluent is nitrogen. The fill pressure P_1 is 30 atm, the temperature of the unburned mixture of gases T_1 is 298 K

From the relation for mass flow rate ($\dot{m} = \rho AV$), the exact flow rates at each time step are computed. The total number of moles of the mixture is computed which is used to calculate the mole fraction of the individual species of the chemical mixture. Using the values for mole fractions, molecular weights of mixture species, fill pressure and temperature we can obtain the density using ideal gas law which in turn is used in the equation of mass flow rate (shown above); which is then converted to molar flow rate $\dot{M}$ by dividing with the Molecular weight of the mixture. Thus the molar flow rate of the mixture is obtained and the individual specie molar flow rates can be obtained by multiplying the above computed molar flow rate with corresponding mole fractions. The molar flow rates of the propellant mixture species (without metal addition) as function of Mach number are listed in Table 4.1.

V(m/s)	M1	P1 (atm)	A	ρ (g/m^3)	ṁ	Ṁ (mol/ms)	Xo2	XN2	XCH4	Ṁo2	ṀN2	ṀCH4
1000	2.778	30	0.001134	22756	25808	1.000	0.200	0.550	0.250	0.200	0.550	0.250
1050	2.917	30	0.001134	22756	27098	1.050	0.200	0.550	0.250	0.210	0.578	0.263
1100	3.056	30	0.001134	22756	28388	1.100	0.200	0.550	0.250	0.220	0.605	0.275
1150	3.194	30	0.001134	22756	29679	1.150	0.200	0.550	0.250	0.230	0.633	0.288
1200	3.333	30	0.001134	22756	30969	1.200	0.200	0.550	0.250	0.240	0.660	0.300
1250	3.472	30	0.001134	22756	32259	1.250	0.200	0.550	0.250	0.250	0.688	0.313
1300	3.611	30	0.001134	22756	33550	1.300	0.200	0.550	0.250	0.260	0.715	0.325
1350	3.750	30	0.001134	22756	34840	1.350	0.200	0.550	0.250	0.270	0.743	0.338
1400	3.889	30	0.001134	22756	36131	1.400	0.200	0.550	0.250	0.280	0.770	0.350
1450	4.028	30	0.001134	22756	37421	1.450	0.200	0.550	0.250	0.290	0.798	0.363
1500	4.167	30	0.001134	22756	38711	1.500	0.200	0.550	0.250	0.300	0.825	0.375
1550	4.306	30	0.001134	22756	40002	1.550	0.200	0.550	0.250	0.310	0.853	0.388
1600	4.444	30	0.001134	22756	41292	1.600	0.200	0.550	0.250	0.320	0.880	0.400
1650	4.583	30	0.001134	22756	42583	1.650	0.200	0.550	0.250	0.330	0.908	0.413
1700	4.722	30	0.001134	22756	43873	1.700	0.200	0.550	0.250	0.340	0.935	0.425
1750	4.861	30	0.001134	22756	45163	1.751	0.200	0.550	0.250	0.350	0.963	0.438
1800	5.000	30	0.001134	22756	46454	1.801	0.200	0.550	0.250	0.360	0.990	0.450

Table 2.1 Molar flow rates of chemical mixture species

2.4.2 Step 2

The pressure and temperature downstream of the normal shock are computed at each time step using the value of the projectile velocity and the pressure arising from isentropic compression ahead of the shock, based on the test section fill pressure and throat area contraction ratio. As previously mentioned, it is assumed that the nose cone does not reach melting temperatures and that the conical shocks do not affect the flow to a large extent until it reaches the position of the normal shock which is assumed to be at the throat of the projectile. Normal shock equations, Eq. (4.2.4)-(4.2.6) are used to compute the properties of the flow downstream of the shock. The schematic for the

regions at which the values of the flow properties are evaluated along the projectile body is shown in Fig. 4.1.

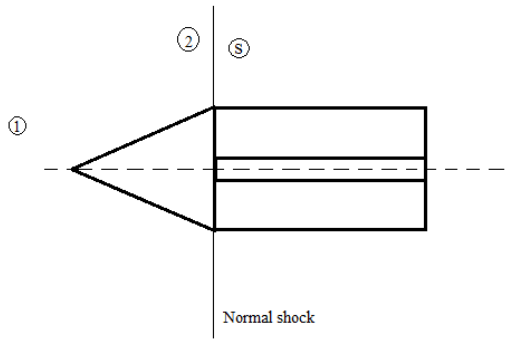

Fig. 2.3 Ram projectile general schematic with normal shock position

For isentropic flow from station '1' to station '2', the relation of Mach number at station '2' M_2 to the incoming Mach number M_1 is obtained as follows:

From continuity equation we have:

$$\dot{m}_1 = \frac{P_1}{RT_1} V_1 A_1 = \dot{m}_2 = \frac{P_2}{RT_2} V_2 A_2$$

$$or\ \frac{\dot{m}_1}{\dot{m}_2} = \frac{P_1}{RT_1}\left(\frac{RT_2}{P_2}\right)\left(\frac{a_1}{a_2}\right)\left(\frac{M_1}{M_2}\right)\left(\frac{A_1}{A_2}\right)$$

$$\therefore 1 = \frac{P_1}{P_2}\frac{T_2}{T_1}\sqrt{\frac{T_1}{T_2}}\left(\frac{M_1}{M_2}\right)\left(\frac{A_1}{A_2}\right) \tag{4.2.1}$$

Also, from the relation for static and stagnation flow properties, we have the following relations:

$$\frac{P_1}{P_2} = \frac{P_{o1}}{P_{o2}}\frac{\left(1+\frac{\gamma-1}{2}M_2^2\right)^{\frac{\gamma}{\gamma-1}}}{\left(1+\frac{\gamma-1}{2}M_1^2\right)^{\frac{\gamma}{\gamma-1}}} \tag{4.2.2}$$

And

$$\frac{T_2}{T_1} = \frac{T_{o2}}{T_{o1}}\frac{\left(1+\frac{\gamma-1}{2}M_2^2\right)}{\left(1+\frac{\gamma-1}{2}M_1^2\right)} \tag{4.2.3}$$

Thus from equation (4.2.1) and using above relations we have

$$1 = \frac{P_{o1}}{P_{o2}}\sqrt{\frac{T_{o2}}{T_{o1}}}\left(\frac{1+\frac{\gamma-1}{2}M_2^2}{1+\frac{\gamma-1}{2}M_1^2}\right)^{\frac{\gamma+1}{2(\gamma-1)}}\left(\frac{M_1}{M_2}\right)\left(\frac{A_1}{A_2}\right)$$

Since we have assumed isentropic flow over the conical nose, no total pressure loss occurs before the throat section and as there is no source of heat addition from station '1' to station '2'. Thus, $P_{o1} = P_{o2}$ and $T_{o1} = T_{o2}$; which gives us the following equation:

$$\left(1+\frac{\gamma-1}{2}M_1^2\right)=\left(1+\frac{\gamma-1}{2}M_2^2\right)\left(\frac{M_1}{M_2}.\frac{A_1}{A_2}\right)^{\frac{2(\gamma-1)}{\gamma+1}}$$

The above expression is solved for M_2 numerically on MATLAB (see the code in Appendix A-section A.1.1).

The flow properties at station '2'; i.e., just before the normal shock, are computed using this Mach number value and the equations (4.2.2) and (4.2.3).

Thus the value for the Mach number at station '2' i.e just before the normal shock is obtained. The Mach number and other flow properties downstream of the shock can then be computed using the normal shock relations as follows (17):

1. The Mach number downstream of the shock is related to the upstream Mach number by

$$M_s^2=\frac{1+\frac{\gamma-1}{2}M_2^2}{\gamma M_2^2-\frac{\gamma-1}{2}} \tag{4.2.4}$$

   Knowing the value of M_2, the Mach number of the flow after the shock is computed easily.

2. The pressure ratio before and after the normal shock is given by

$$\frac{P_s}{P_2}=1+\frac{2\gamma}{\gamma+1}(M_2^2-1) \tag{4.2.5}$$

   As before, knowing the value of P_2, the pressure after the shock is computed.

3. Similarly, the temperature downstream of the shock T_s is obtained from

$$\frac{T_s}{T_2}=1+\frac{2(\gamma-1)}{(\gamma+1)^2}\left(\frac{\gamma M_2^2+1}{M_2^2}\right)(M_2^2-1) \tag{4.2.6}$$

   For the considered sample case, the following table gives the flow properties at stations '2' and station 's' which is downstream of the normal shock as shown in Table 4.2 below:

V(m/s)	M1	P1 (atm)	To1	Po1	Ms	Ts	Ps
1000	2.778	30	717	805	0.6000	660	424
1050	2.917	30	759	1002	0.5680	701	478
1100	3.056	30	804	1244	0.5440	742	531
1150	3.194	30	851	1541	0.5240	784	585
1200	3.333	30	900	1904	0.5086	828	614
1250	3.472	30	951	2345	0.4950	874	698
1300	3.611	30	1004	2879	0.4830	921	757
1350	3.750	30	1059	3524	0.4730	971	818
1400	3.889	30	1117	4300	0.4650	1022	881
1450	4.028	30	1176	5230	0.4570	1075	945
1500	4.167	30	1238	6340	0.4500	1129	1010
1550	4.306	30	1301	7660	0.4400	1187	1080
1600	4.444	30	1367	9225	0.4300	1241	1145
1650	4.583	30	1434	11073	0.4300	1301	1217
1700	4.722	30	1504	13250	0.4300	1363	1292
1750	4.861	30	1576	15805	0.4200	1427	1368
1800	5.000	30	1650	18795	0.4200	1493	1446

Table 2.2 Flow properties downstream of the normal shock

2.4.3 Step 3

The NASA CEA code which has been modified for TCRA applications is used (18). The input is the chemical composition of the mixture at each time step and the corresponding value of temperature and pressure downstream of the normal shock.

All the properties of the flow and molar flow rates obtained in steps 1 and 2 are used as input to the TCRA CEA code for each time step. Values of kinematic viscosity, specific heat at constant pressure and Prandtl number are obtained in the output of the TCRA CEA code. A representative output file can be found in Appendix A (Section A.4). The transport properties obtained are as shown in Table 4.3.

V(m/s)	M1	μ (Ns/m2)	Cp (kJ/kg-K)	Pr
1000	2.778	NA	NA	NA
1050	2.917	NA	NA	NA
1100	3.056	NA	NA	NA
1150	3.194	NA	NA	NA
1200	3.333	NA	NA	NA
1250	3.472	NA	NA	NA
1300	3.611	770.7	1.945	0.5643
1350	3.750	779.5	1.949	0.5636
1400	3.889	789.4	1.954	0.5627
1450	4.028	800.8	1.958	0.562
1500	4.167	811.5	1.963	0.5614
1550	4.306	655.9	1.883	0.5605
1600	4.444	836.2	1.971	0.5599
1650	4.583	848.8	1.977	0.559
1700	4.722	862.6	1.981	0.5583
1750	4.861	877.2	1.985	0.5577
1800	5.000	890.0	1.991	0.5566

Table 2.3 Transport properties of the flow

2.4.4 Step 4

The heat coefficient values are then computed using the Bartz equation using the transport properties obtained in Step 3.

The Bartz equation for the heat coefficient is (19) (20):

$$h_{Bartz} = \left[\frac{0.026}{D_t^{0.2}}\left(\frac{\mu^{0.2}C_p}{P_r^{0.6}}\right)\left(\frac{P_c g}{c^*}\right)^{0.8}\left(\frac{D_t}{R}\right)^{0.1}\left(\frac{A_t}{A}\right)^{0.9}\sigma\right]$$

In this equation (21),

$$\sigma = \frac{1}{\left\{\left[\frac{T_w}{2T_o}\left(1+\frac{\gamma-1}{2}M^2\right)+\frac{1}{2}\right]^{0.68}\left(1+\frac{\gamma-1}{2}M^2\right)^{0.12}\right\}} \text{ and } c^* = \sqrt{\frac{RT}{\gamma}}\left(\frac{\gamma+1}{2}\right)^{\frac{\gamma+1}{2(\gamma-1)}}$$

In the above equation for the heat transfer coefficient, C_p is the specific heat at constant pressure, P_r is the Prandtl number, D_t is the diameter of the throat, A_t is the area at the throat, A is the area of the bore or tube, P_c is the chamber pressure, T_w is the temperature of the projectile wall, T_o is the stagnation temperature in the boundary layer around the projectile, M is the mach number of the flow and γ is the ratio of specific heats.

The following Table 4.4 shows the values for the heat transfer coefficients at each time step for the 38-mm-bore diameter with aluminum projectile:

V(m/s)	M1	μ (Ns/m2)	Cp (kJ/kg-K)	Pr	H_Bartz (10^6)
1000	2.778	NA	NA	NA	NA
1050	2.917	NA	NA	NA	NA
1100	3.056	NA	NA	NA	NA
1150	3.194	NA	NA	NA	NA
1200	3.333	NA	NA	NA	NA
1250	3.472	NA	NA	NA	1.347
1300	3.611	770.7	1.945	0.5643	1.403
1350	3.750	779.5	1.949	0.5636	1.495
1400	3.889	789.4	1.954	0.5627	1.588
1450	4.028	800.8	1.958	0.562	1.682
1500	4.167	811.5	1.963	0.5614	1.775
1550	4.306	655.9	1.883	0.5605	1.872
1600	4.444	836.2	1.971	0.5599	1.964
1650	4.583	848.8	1.977	0.559	2.061
1700	4.722	862.6	1.981	0.5583	2.159
1750	4.861	877.2	1.985	0.5577	2.258
1800	5.000	890.0	1.991	0.5566	2.358

Table 2.4 Heat transfer coefficients at each time step

2.4.5 Step 5

As previously discussed, the projectile is assumed to have a cylindrical body with rectangular fins as shown below in Fig. 4.2. The nose cone heat transfer is ignored since the normal shock is assumed to be located at the throat of the projectile. From steps 1-3 and using the heat coefficient as obtained from the above step 4 and the film temperature of the boundary layer formed over the projectile in ANSYS Thermal Transient module, the amount of the metal which reaches melting temperature and is then swept away at each step is estimated.

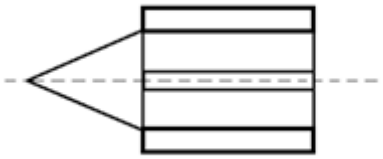

Fig. 2.4 General projectile design schematic

The projectile can be divided into cylindrical and fin portions and analyzed on ANSYS individually. The cylindrical part is modeled as a 2D object on ANSYS. The details of the geometry, mesh, mesh controls, analysis settings and the thermal load settings for the cylindrical body and the fins can be found in Appendix A.

The estimates for the amount of molten metal were made from the temperature plots obtained from ANSYS. It is assumed that the layer which reaches the melting temperature is swept away from both the projectile body and the fin surfaces immediately as a result of the aerodynamic shear stresses.

The temperature contour plot for Mach 4.306 of the cylindrical part of the projectile is shown in Fig. 4.3. This is obtained at 0.5 ms from the beginning of the thermal transient analysis and shows that the maximum temperature (of the outermost layer) is 1246 K which is above the melting point (~923 K) of the aluminum projectile body. Fig. 4.4 shows the zoomed in view of the temperature contours for the cylindrical part of the projectile. The layer which attains a temperature just above the melting temperature of aluminum is estimated from this plot and knowing the meshing properties, the amount of aluminum which ablates is calculated.

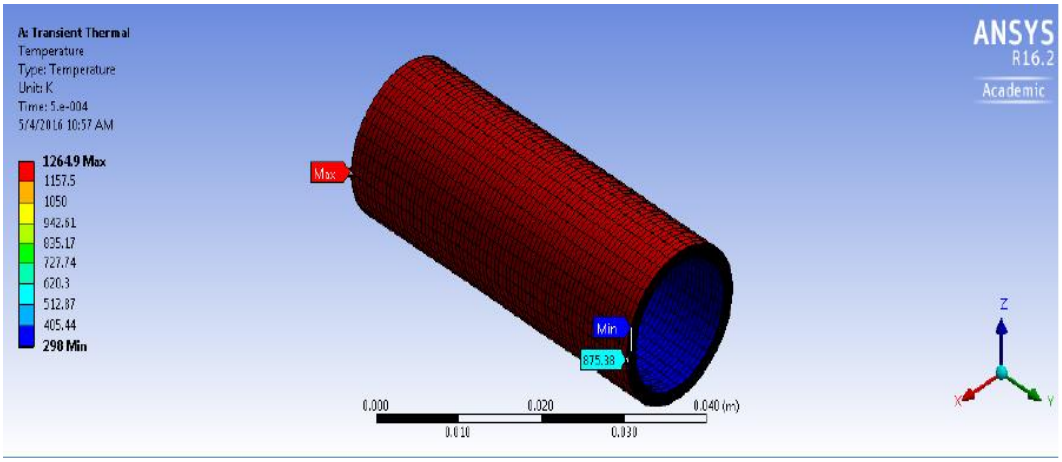

Fig. 2.5 ANSYS cylindrical body transient thermal result

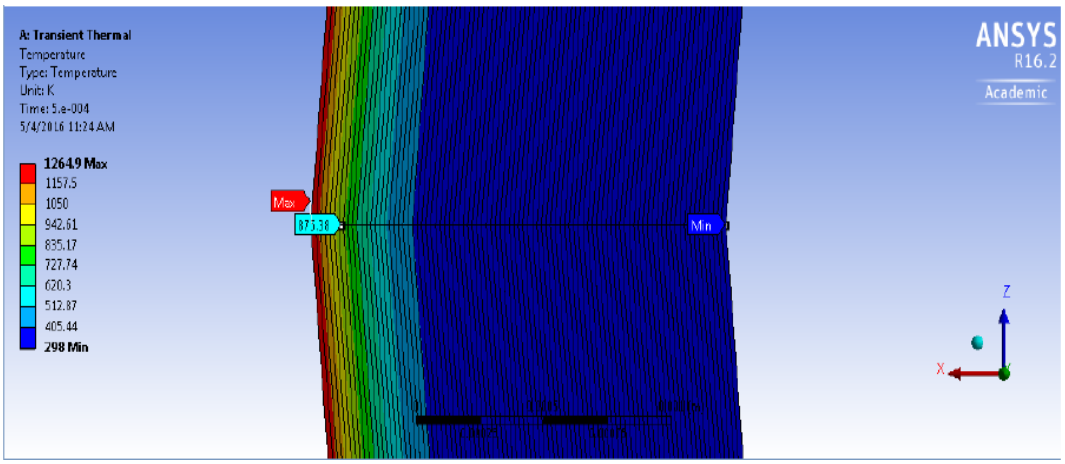

Fig. 2.6 ANSYS cylindrical body temperature gradient

Similar estimates can be obtained for the fins from their internal temperature distribution as shown in Fig. 4.5, which is again for Mach 4.306. It is clear from this figure that the maximum temperature of the outermost layer of the fin is greater than that of the cylindrical part of the projectile and thus the amount of metal which ablated from the fins cannot be ignored.

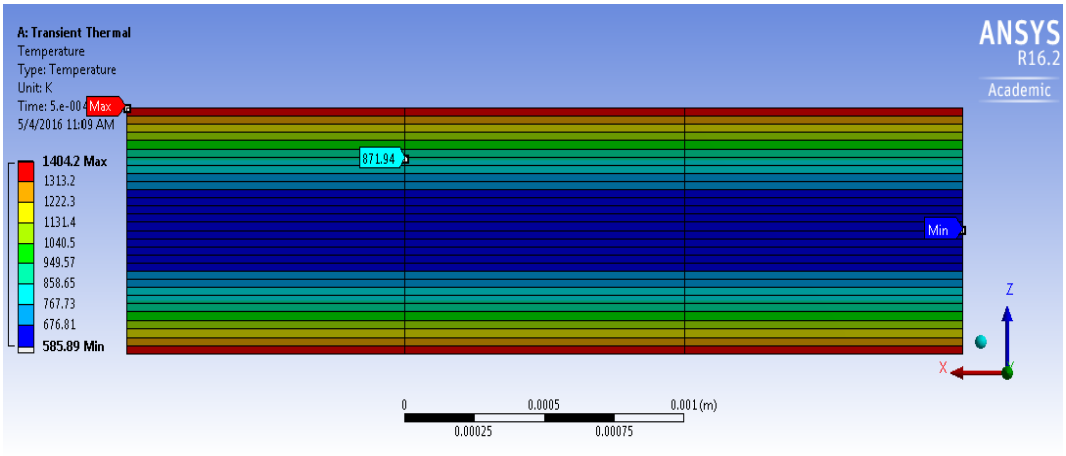

Fig. 2.7 ANSYS projectile fin temperature gradient

The total amount of molten metal is obtained by adding up the estimates from cylindrical part of the projectile and that from the fins. This metal is in a molten state and not a gaseous phase. The approach for determining the fraction of the metal that is available in gaseous phase for reaction with other gases in the tube is described in step 6.

2.4.6 Step 6

As described in step 5, the amount of metal that melts off from the projectile is in liquid phase and the temperature around the projectile is not sufficient to vaporize all the metal in liquid state. The actual amount of metal that gets vaporized can be estimated by using the constant enthalpy calculations of the NASA CEA code. This is achieved by comparing the adiabatic flame temperatures for the initial gaseous molar flow rates and the amount of the molten metal added in moles at stagnation temperature due to aerodynamic heating with the adiabatic flame temperature for the initial gaseous molar flow rates of the mixture and the same amount of molten metal now assumed to be in a gaseous phase at room temperature. The temperatures of the components of the mixture other than the metal are maintained at the stagnation temperature.

The amount of metal in the gaseous state is adjusted until the adiabatic flame temperatures of the two reaction cases described above are within a reasonable range (25 K difference) further discussed in the chapter on results. Thus the amount of metal from the projectile that gets transformed into gaseous phase and is available for reaction with the fuel (methane) and the oxidizer (oxygen) is estimated. This new amount estimated is significantly less than the amount (in moles) of the molten metal sometimes less by more than 50%. Thus the energy balance in the whole setup is accounted for and gives the most accurate non dimensional thrust profiles.

2.4.7 Step 7

As described in steps 1-6, once the amount of gaseous metal added to the flow at every time step is obtained, the TCRA CEA code is used to obtain the non dimensional thrust coefficients at each step. The exact non-dimensional thrust coefficient is read off from the graphs of the non-dimensional thrust coefficient profiles at the Mach numbers corresponding to each time step and the non-dimensional thrust coefficient profile of the ram shot accounting for the melting metal is obtained as shown in the chapter on results.

Fig. 4.6 shows the thrust profiles for the ablation model for the Mach numbers 4.028, 4.167 and 5. The corresponding thrust coefficients are read off from the graph and these are tabulated as shown in Table 4.5. This procedure is repeated for all the Mach number resolutions available.

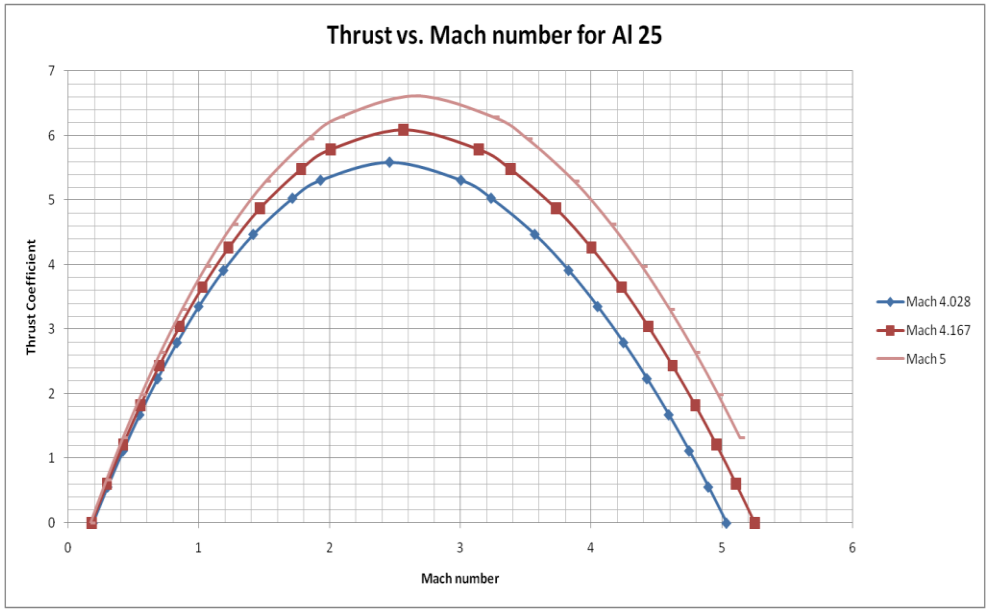

Fig. 2.8 Al 25 mm Thrust vs. Mach number for M- 4.028, 4.167 and 5

Mach number	Non- dimensional thrust coefficient
4.028	3.4
4.167	4
5	2

Table 2.5 Mach number and corresponding non-dimensional thrust coefficient

2.4.8 Step 8

The non-dimensional thrust coefficient profile for the ram shots accounting the melting of the projectile body due to very high temperatures and pressures is obtained as described in step 7. The

profile is separated in two parts, i) The profile for combustion of the mixture until the addition of metal from the projectile body initiates and ii) the non-dimensional thrust coefficient profile for combustion of the initial mixture and the metal added to the flow as fuel.

A curve fit is used on the profile to get a model (or function of Mach number). This fit can be a 2^{nd} order curve to account for the 2^{nd} degree relation between the non-dimensional thrust coefficient and the Mach number or the 3^{rd} order fit so that the error is reduced for a perfect match. These models are then used in the forward Euler algorithm on MATLAB (see appendix for code) to obtain the velocity-distance profiles for the specified mixture, size of projectile and the ram tube bore diameter at their respective fill pressures. The step size is set to 0.05 so that changing the size by a factor of ten produces a result which does not vary more than 1%.

Chapter 3 Experimental Facility

3.1 University of Washington Facility

The ram accelerator facility at the University of Washington, from which the archived experimental data for comparison of the proposed ablation model is taken, is as shown in Fig. 4.1 (2). It consists of a light gas gun pre-launcher, ram accelerator test section, final dump tank and the catcher tube. The pre-launcher is a 6-m-long, 38-mm-bore helium gas gun which is capable of launching a projectile to supersonic speeds (up to 1.3 km/s). The ram accelerator itself is a 16-m-long tube consisting of eight 2-m-long sections of steel joined by threaded collars. Nearly 2000 ram accelerator experiments have been carried out in this facility to examine operating characteristics over the velocity range of 600 to 2700 m/s and in-tube Mach number range of 2.2 to 8.5.

The tubes are typically filled with 20-50 atm of combustible mixture. The chemical composition of the mixture is adjusted by simultaneously routing the component gases through individually controlled mass flow meters which mix the gases as they co-flow through the fill line of the test section (22). Thin Mylar diaphragms are inserted at selected tube joints to separate propellant gases in the test section. Since the diaphragms may be placed at any joint, the mixture chemistry in the test section may be changed along the length of the tube to control in-tube Mach number.

To track the projectile and examine the flow field, the test section has instrument stations at 40 cm intervals along its length. Each station has either 3 or 4 instrument ports into which a variety of pressure, magnetic or optical sensors may be inserted. All the sensors are recessed slightly (about 0.5 mm) from the tube wall to prevent impact damage due to the passing projectile. The magnetic sensors provide the time history of the projectile in the tube by tracking a magnetic ring. This ring is carried on the projectile at the throat, where the nose and the body meet (23).

The nose and the body of the projectile are machined separately and the hollow pieces are threaded together at the throat. This hollow design serves to minimize the projectile mass, enabling high accelerations at relatively low gas pressures. Normally, projectiles are machined from magnesium (ZK60 AT5) or aluminum (7075 T6) alloys. Projectile masses vary from 60-130 g (24), depending on the material and the internal dimensions of the design. The projectile body is manufactured with integral fins, which center the projectile as it travels down the tube.

3.2 The 90 mm Ram Accelerator in France

In addition to the analysis of the data of the 38-mm-bore facility at the University of Washington, the data (25) obtained from the 90-mm-bore ram accelerator facility in France is also analyzed in this thesis (26). This facility was constructed at the French- German Research Institute of Saint-Louis (ISL), France, using military 90-mm cannon as a pre-launcher. Entrance velocity was usually 1.4 km/s and exit velocities up to 2.4 km/s were achieved here in its (27-m-long test) section in multi-stage experiments. The projectiles were made of aluminum alloy weighing from 1.2-1.4 kg and the typical fill pressure was about 40 atm. Schematic for this facility is shown in Fig. 4.3 (27).

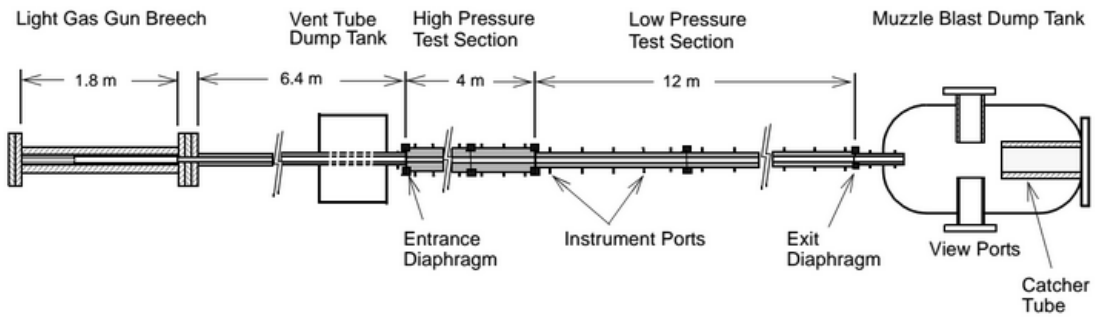

Fig. 3.1 University of Washington 38-mm-bore ram accelerator facility

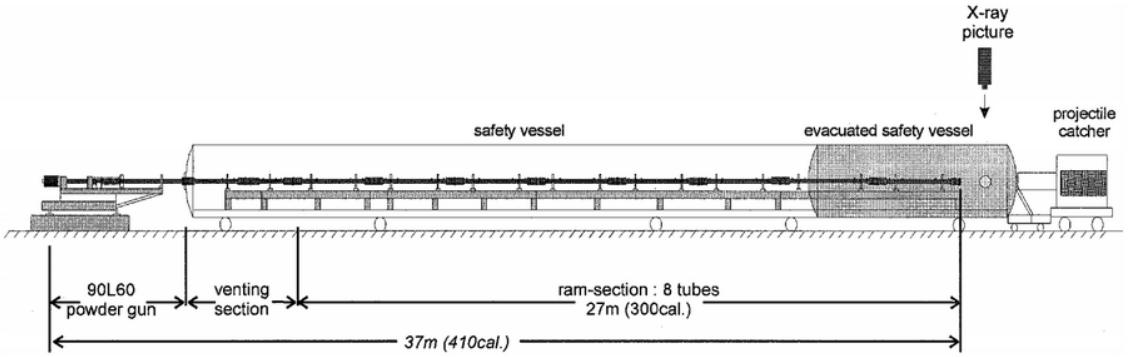

Fig. 3.2 Institute of Saint Louis 90-mm-bore ram accelerator facility

3.3 The 25 mm Ram Accelerator in Japan

Another set of data (28), (29) analyzed in this thesis is from the 25-mm-bore ram accelerator facility at Tohoku University in Sendai, Japan (18). Low mass, high acceleration tests were carried out with entrance velocity around 1100 m/s and exit velocities up to 2.4 km/s were achieved in the 6.6 m long test section. This facility also had provisions for high speed photography. The projectiles were made of aluminum alloy, weighing from 18-23 g and the typical fill pressures ranged from 25-35 atm. A schematic of this facility is shown in Fig. 4.2 (30).

Fig. 3.3 Shock Wave Research Center, Tohoku University 25-mm-bore ram accelerator

Chapter 4 Results

4.1 NASA CEA- HP Calculations

Melting and vaporization properties of various pure metals are listed in Table 4.1. The ablated metal from the projectile at any given Mach number that was determined from the modeling procedure is assumed to mix with the flow in a molten state. If the static temperature of the flow is greater than the vaporization temperature, then the flow total temperature is reduced by the amount required to vaporize all the molten metal prior to combustion and the reactants can be consider gaseous in the subsequent thermo-chemical calculations. Turns out this only applied to magnesium in this study because its vaporization temperature is relatively low (1383 K).

Metal (pure)	Heat Capacity (kJ/kg/K)	Melting Temperature (K)	Latent Heat of Melting (kJ/kg)	Vaporization Temperature (K)	Latent Heat of Vaporization (kJ/kg)
Magnesium	1.020	923	368	1383	5270
Aluminum	0.897	932	399	2600	10530
Titanium	0.523	1973	419	3533	8960

Table 4.1 Physical properties of various metals at 1 atm

To account for partial vaporization of metal in the flow, the NASA CEA-hp calculations were utilized. This module of the NASA CEA code calculates all the equilibrium properties based on constant enthalpy and constant pressure assumption while handling mixed phase reactants. In this manner, the adiabatic flame temperature is determined for the state of the flow at various Mach numbers based on the following assumptions:

1. The ablated metal is in liquid phase with temperature equal to the total temperature of the flow.
2. The ablated metal is in gaseous phase at room temperature (298 K).

Assuming that the amount of combustion heat release is about the same in both cases, the difference in adiabatic flame temperatures obtained must correspond to the difference in the amount of liquid and gaseous phase ablated metal in reactants. Thus, the amount of moles of the metal are adjusted in the gaseous phase until the adiabatic temperatures are nearly equal (tolerance of 25 K is considered as the value for the amount of metal do not vary much up to this temperature difference). For the case of flow at Mach 4.306 with molten aluminum added to the flow, Table 5.1 shows the values of the adiabatic flame temperatures reached with corresponding amount of the ablated metal in the flow. The output file from the NASA CEA-hp module for this sample case is attached in the Appendix A (Section A.2). These results indicate that TCRA performance parameters can be predicted by assuming ~ 56% of the aluminum is participating in the combustion.

Mixture: $2.7CH_4 + 2O_2 + 5.8N_2$, Mach number of the flow is 4.306		
Description	**Adiabatic flame temperature (K)**	**Amount of ablated metal (moles)**
Liquid phase at 1301 K	2720	0.1433
Gaseous phase at 298 K	3039	0.1433
Gaseous phase at 298 K	2723	0.08

Table 4.2 **Adiabatic flame temperatures of Al in different conditions**

4.2 Number of Moles of Metal Added as a Function of Mach Number

As a representative case for the 38-mm-bore ram accelerator, a projectile made of aluminum having 4 fins and throat diameter of 29 mm and the length and thickness of the projectile wall being 71 mm and 3 mm, respectively, is considered here. The number of moles of ablated metal in molten and vapor states, as determined by evaluating liquid and gaseous aluminum addition on adiabatic flame temperature as discussed above, are shown in Fig. 4.1. The ablation model predicts that the metal will start melting at Mach ~ 3.9 in this case and that only a fraction of the ablated metal is converted to gaseous phase.

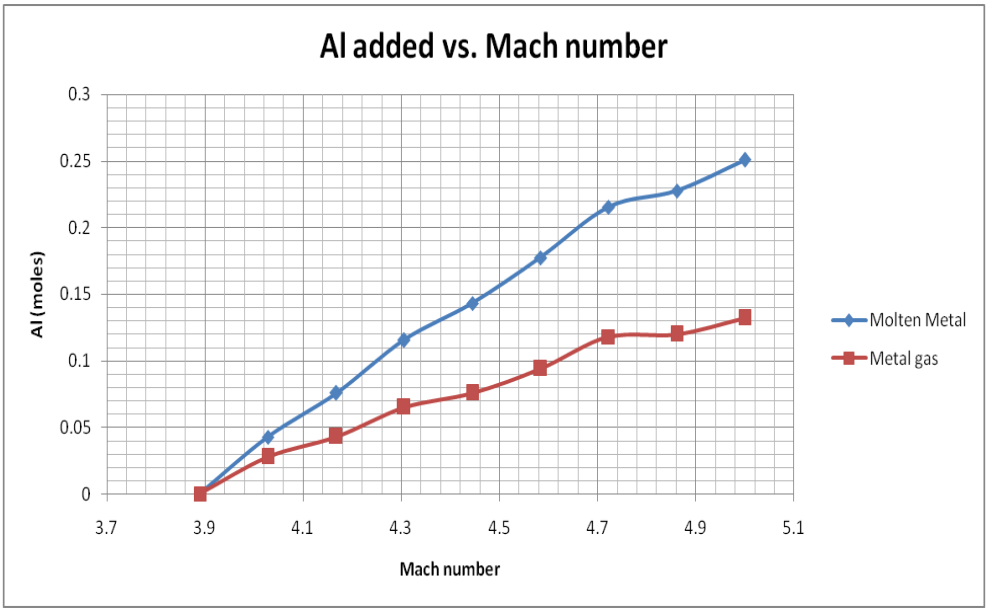

Fig. 4.1 **38 mm bore Al projectile- amount of metal added to the flow**

A second sample case considered in 38-mm-bore ram accelerator is considered here, where the projectile is made of magnesium having 4 fins and throat diameter of 29 mm and the length and thickness of the projectile wall being 71 mm and 3 mm, respectively. The number of moles of ablated magnesium in molten and vapor states are shown in Fig. 4.2. The ablation model predicts that the metal will just start to melt at Mach ~ 3.9 in this case.

Additional cases involving titanium projectiles were examined, however, there was negligible ablation predicted over the range of Mach numbers considered. This numerical result is consistent with experiment in that the onset of enhanced thrust, with respect to the thermally choked propulsive model, is not observed until the projectile reaches ~95% CJ speed. Thus the analytical results from modeling these experiments were not reported here.

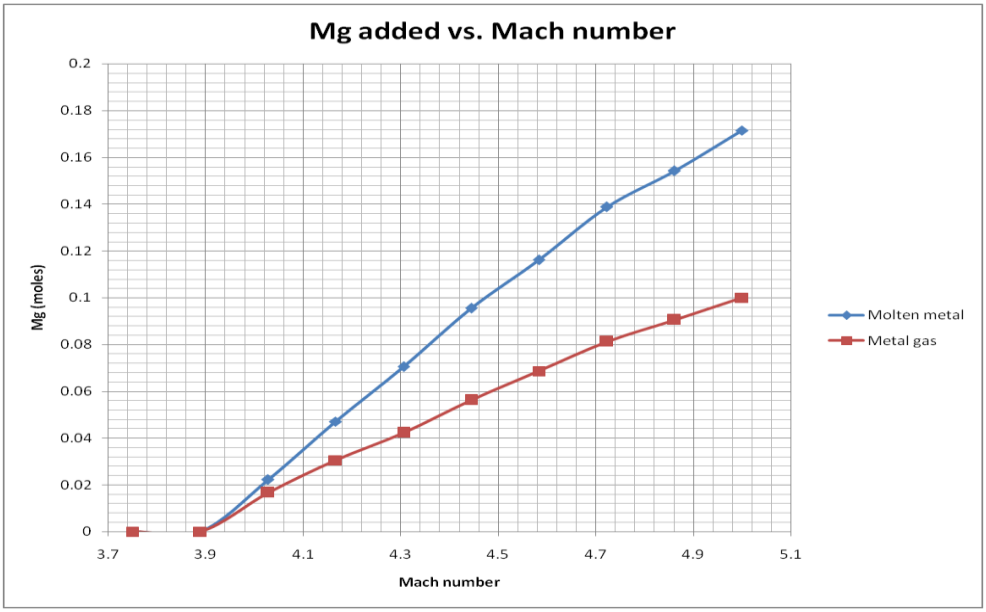

Fig. 4.2 38 mm bore Mg projectile- amount of metal added to the flow

For the mixture $2.8CH_4 + 2O_2 + 5.7N_2$ with the bore diameter of 25 mm, Fig. 4.3 shows the amount of ablated aluminum in molten vs. gaseous phase. The projectile has a throat diameter of 19 mm and length of 47 mm with the wall thickness being 2 mm with 4 fins with same wall thickness as the projectile aftbody. In this case the onset of ablation is again predicted to occur at Mach ~ 3.9, all be it with a lower molar loss rate as expected from less exposed surface area.

For the 90-mm-bore ram tube case considered here with the chemical mixture of $3CH_4 + 2O_2 + 9.7N_2$, the projectile was made of aluminum with throat diameter of 68 mm, length and wall thickness being 168 mm and 7 mm, respectively. Fig. 4.4 shows the molar amount of the ablated aluminum predicted to be in two different phases as function of Mach number. In this case it is predicted that the ablation begins above Mach 4.0, and that the molar amount of aluminum introduced to the flow via ablation is substantially higher than in the smaller bore ram accelerators, which is consistent with the much greater external surface area of the 90-mm projectiles.

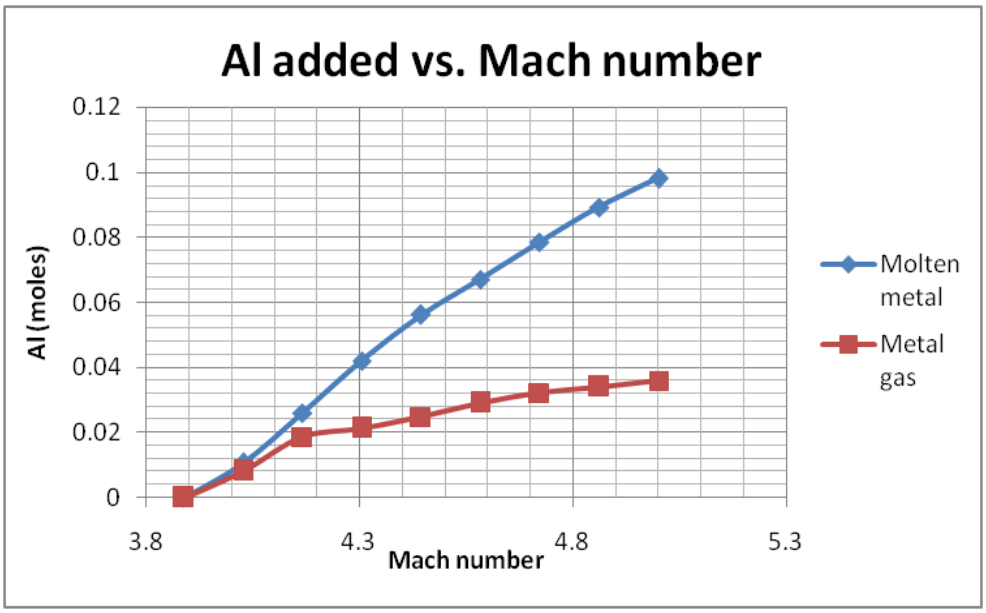

Fig. 4.3 25 mm bore Al projectile- amount of metal added to the flow

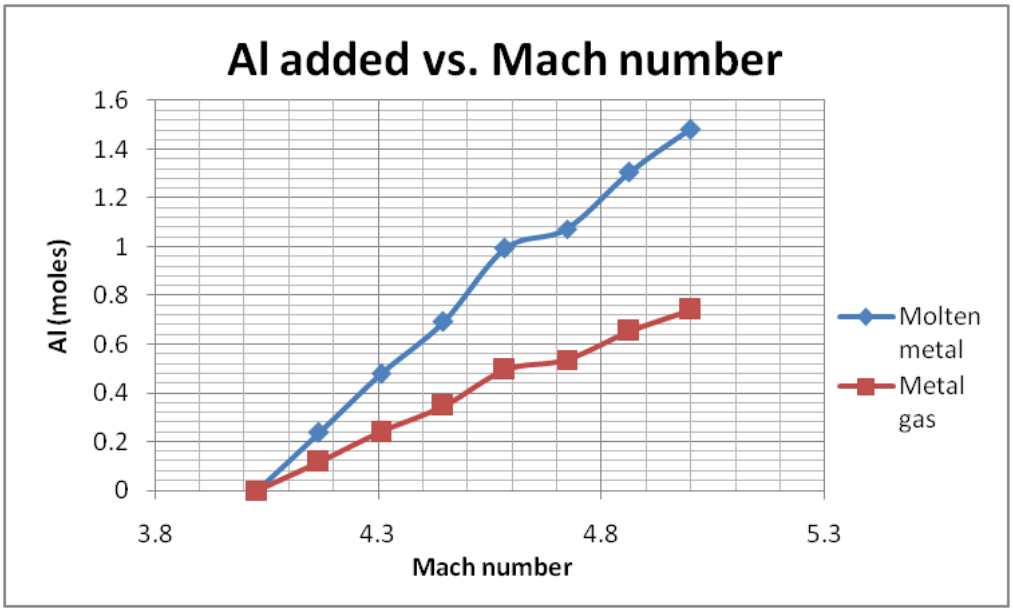

Fig. 4.4 90 mm bore Al projectile- amount of metal added to the flow

4.3 Non-Dimensional Thrust Coefficient Profile with Respect to Mach Number

For the sample case considered with mixture $2.7CH_4 + 2O_2 + 5.8N_2$, tube bore diameter- 38 mm and projectile being: metal-aluminum, fins- 4, throat diameter- 29 mm, length- 71 mm, thickness- 3 mm, Fig. 4.5 shows the thrust-Mach number profile. The thrust is predicted to start deviating from the nominal theoretical profile with no aluminum addition at about Mach 4, and even increases with increasing Mach before attaining a relative maximum at Mach ~ 4.2 and subsequently decreasing.

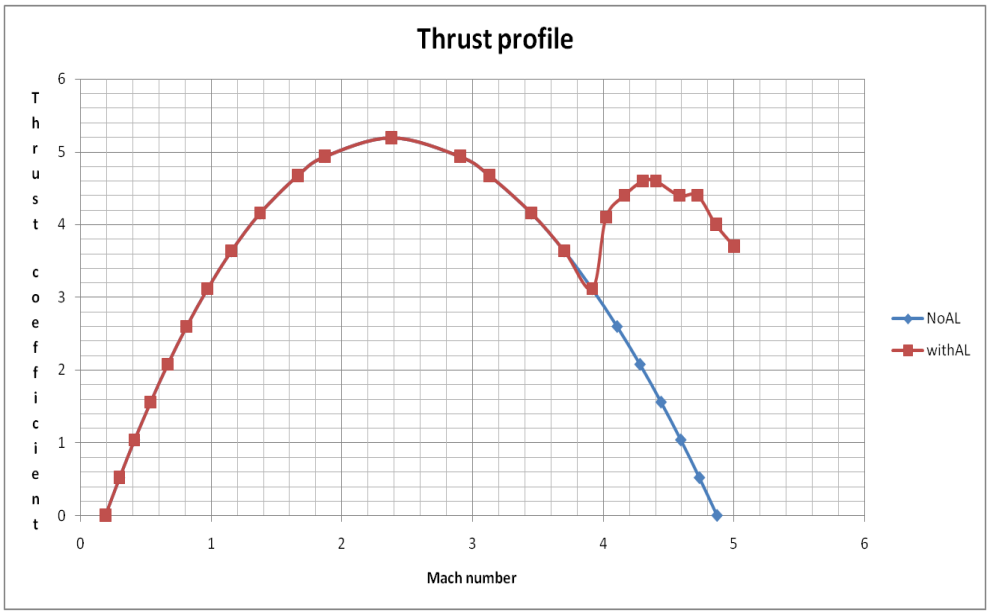

Fig. 4.5 38 mm bore Al projectile thrust profile

The thrust-Mach number profile predicted for the propellant mixture $2.7CH_4 + 2O_2 + 5.8N_2$, tube bore diameter-38 mm and the projectile details being: metal- magnesium, fins- 4, diameter-29 mm, length- 71 mm, thickness- 3 mm is shown in Fig. 4.6. The thrust is predicted to begin deviating from the theoretical curve at around Mach 3.9 and again increasing to a relative maximum at Mach 4.2.

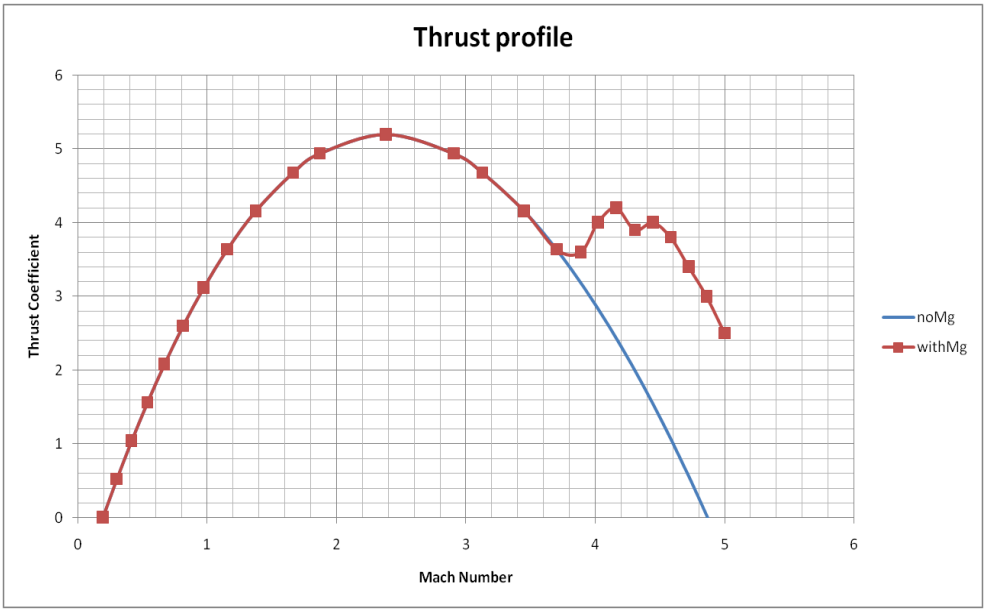

Fig. 4.6 38 mm bore Mg projectile thrust profile

The predicted thrust-Mach profile with propellant mixture $2.8CH_4 + 2O_2 + 5.7N_2$ and tube bore of 25 mm with projectile details being: metal-aluminum, fins- 4, throat diameter-19 mm, length-

47 mm, thickness- 2 mm is shown in Fig. 4.7. Deviation from theory without metal addition is predicted to begin at Mach ~ 3.8 and a relative maximum is reached at Mach ~ 4.2, in a manner similar to that seen in Fig. 4.5.

The predicted thrust-Mach profile with propellant mixture $3CH_4 + 2O_2 + 9.7N_2$ and tube bore of 90 mm with a projectile made of aluminum having 4 fins, throat diameter of 68 mm, body length being 362 mm and the wall thickness of 7 mm is shown in Fig. 4.8. The influence of ablation becomes evident at Mach numbers greater than 4. Note the propellant chemistry used here has more N2 diluent than that used in the smaller bore systems, thus it has a lower CJ speed Mach. The subsequent relative maximum in thrust occurs around Mach 4.3 in this case.

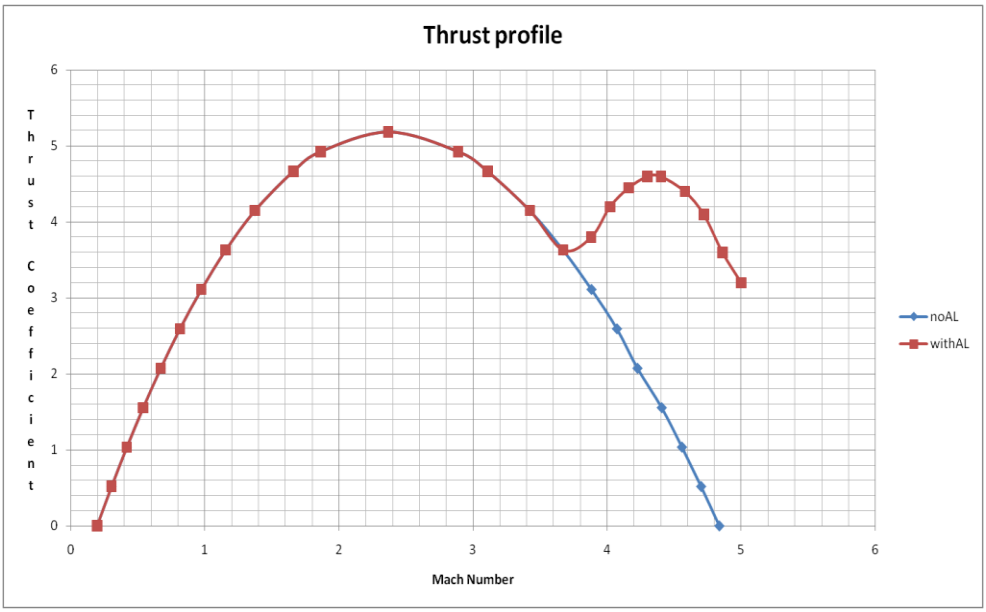

Fig. 4.7 25 mm bore Al projectile thrust profile

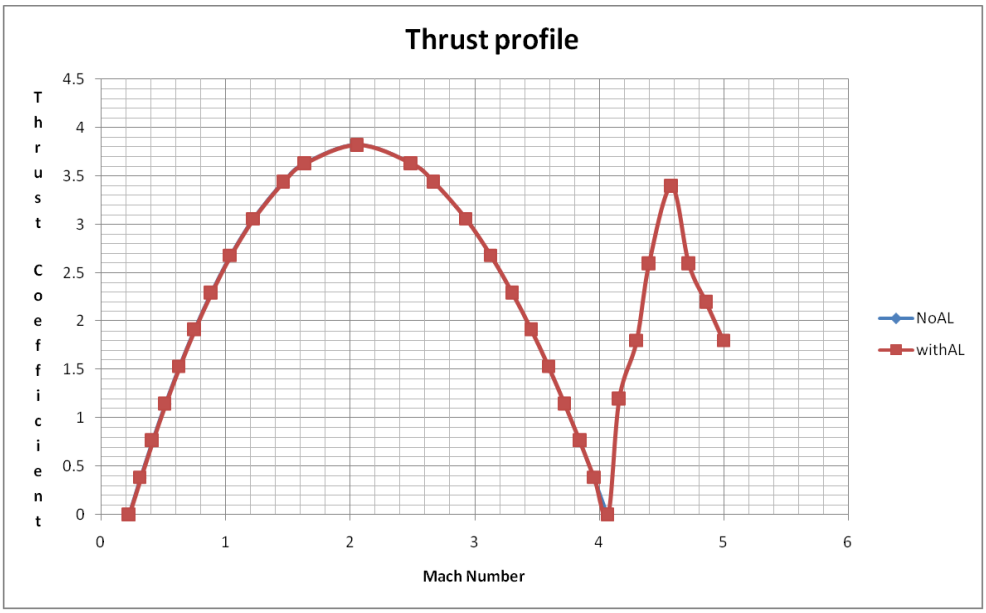

Fig. 4.8 90 mm bore Al projectile thrust profile

4.4 Velocity-Distance Profiles

For the sample case considered with mixture $2.7CH_4 + 2O_2 + 5.8N_2$, tube bore diameter-38 mm and projectile detail being: metal-aluminum, fins- 4, throat diameter- 29 mm, length- 71 mm, thickness- 3 mm, Fig. 4.9 shows the predicted velocity-distance profile for a projectile having an initial mass 70 g in propellant at fill pressure 30 atm. The theoretical curve for pure gaseous propellant indicates that a velocity of ~1720 m/s is attained in 10 m of operation, whereas the thrust enhancement resulting from including the effects of combusting the ablated aluminum results in a predicted peak velocity of 2070 m/s in the same distance. The onset of ablation is evident by the deviation of the curves at a distance of ~2.5 m in this case.

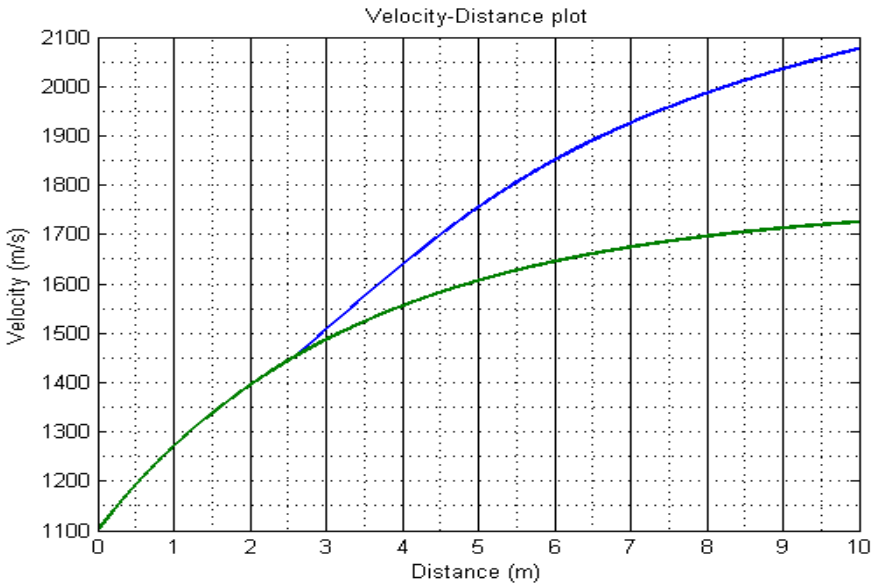

Fig. 4.9 38 mm Al projectile velocity distance profile

Fig. 4.10 shows the velocity-distance profile for the case with mixture $2.7CH_4 + 2O_2 + 5.8N_2$, tube bore diameter-38 mm and the projectile details being: metal- magnesium, fins- 4, diameter- 29 mm, length- 71 mm, thickness- 3 mm. The projectile has an initial mass of 60 g and the fill pressure is 30 atm. The theoretical curve for pure gaseous propellant indicates that a velocity of ~1750 m/s is attained in 10 m of operation, whereas the thrust enhancement resulting from including the effects of combusting the ablated magnesium results in a predicted peak velocity of 1950 m/s in the same distance. The onset of ablation is evident by the deviation of the curves at a distance of ~2.25 m in this case.

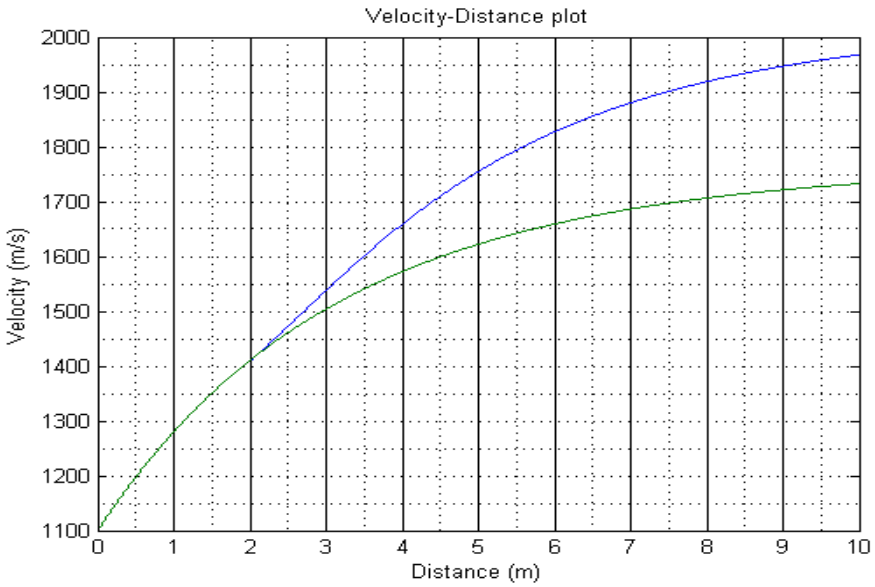

Fig. 4.10 38 mm Mg projectile velocity distance profile

The case with mixture $2.8CH_4 + 2O_2 + 5.7N_2$ and tube bore diameter-25 mm with projectile details being: metal-aluminum, fins- 4, throat diameter-19 mm, length- 47 mm, thickness- 2 mm is seen in Fig. 4.11. The projectile has an initial mass of 20 g and the fill pressure is 35 atm. The theoretical curve for pure gaseous propellant indicates that a velocity of ~1750 m/s is attained in 10 m of operation, whereas the thrust enhancement resulting from including the effects of combusting the ablated aluminum results in a predicted peak velocity of 2050 m/s in the same distance. The onset of ablation is evident by the deviation of the curves at a distance of ~1.5 m in this case.

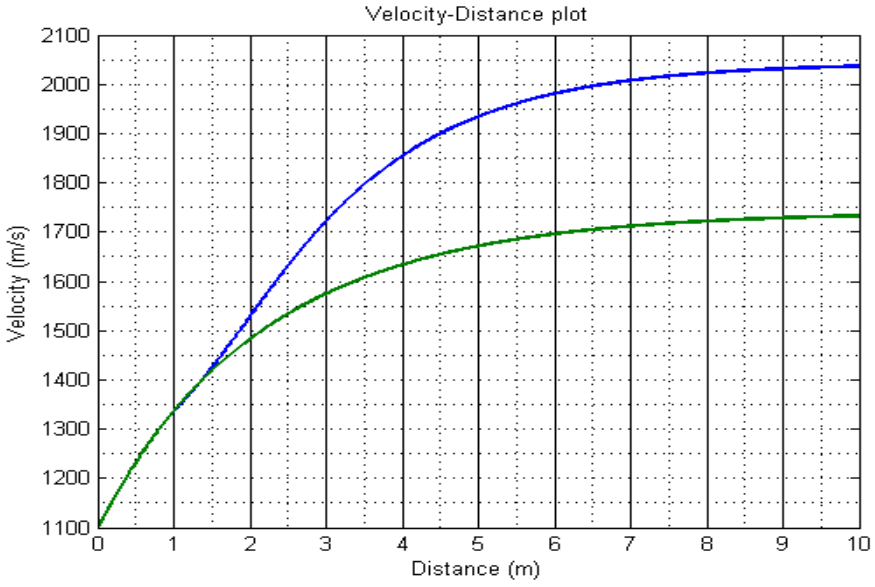

Fig. 4.11 25 mm Al projectile velocity distance profile

For the 90-mm-bore ram tube with the chemistry being $3CH_4 + 2O_2 + 9.7N_2$ and the projectile made of aluminum with 4 fins and the throat diameter of 68 mm with length being 362 mm and the wall thickness of 7 mm, the velocity-distance profile is shown in Fig. 4.12. The projectile has an initial mass of ~1 kg and the fill pressure is 40 atm. The theoretical curve for pure gaseous propellant indicates that a velocity of ~1465 m/s is attained in 15 m of operation, whereas the thrust enhancement resulting from including the effects of combusting the ablated aluminum results in a predicted peak velocity of 1550 m/s in the same distance. The onset of ablation is evident by the deviation of the curves at a distance of ~10 m in this case.

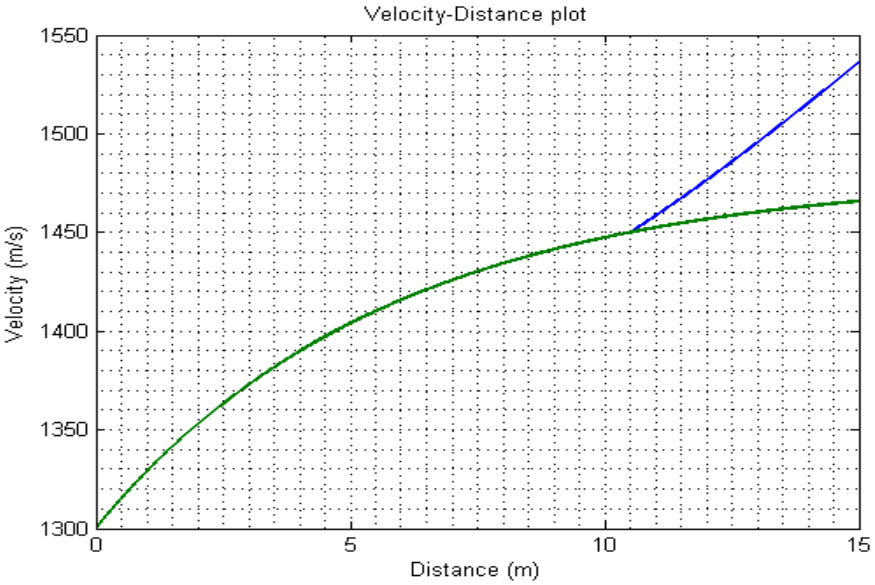

Fig. 4.12 90 mm Al projectile velocity distance profile

4.5 Comparison of Experimental and Ablation Model Velocity-Distance Profiles

The ablation model developed here is applied to the archived data from the experimental ram accelerator shots obtained from the ram accelerator facilities at UW, ISL and the Tohoku University. The one dimensional theoretical model without ablation is also compared in these plots. Fill pressures and initial velocities from the experimental data are used to modify the ablation model to correspond with the individual experimental run data. The run numbers for the runs analyzed are mentioned at the top of the graphs.

4.5.1 Velocity-distance profile for 38-m-bore ram accelerator

The comparison for the experiment vs. the ablation model velocity-distance profiles for 38-mm-bore ram accelerator for a few particular runs is shown in this section. Fig. 4.13 shows the velocity-distance plot for run number HS826 for a projectile made of aluminum, for the mixture

$2.7CH_4 + 2O_2 + 5.8N_2$, tube bore diameter- 38 mm and projectile details for the model being: fins- 4, throat diameter- 29 mm, length- 71 mm, thickness- 3 mm with initial mass being 72.4 g and fill pressure 25 atm. For this run, the ablation initiation velocities (ablation initiation velocity is defined as the velocity of the chemical mixture over the projectile at which the ablation of the projectile is first observed) in theory and experiment differ by ~14 %; the ablation initiation velocity for the experiment is ~1700 m/s and that for the ablation model is 1462 m/s. The ablation initiation distances vary by ~5 m. The slope of the theoretical velocity-distance data was much steeper than experiment, indicating that thrust was over predicted in this velocity range. Note the CJ speed of this propellant is 1760 m/s, thus the onset of enhanced thrust was not evident until the projectile had almost reached CJ speed.

Fig. 4.14 shows the velocity-distance profile for the run HS1000 in which the projectile was made of magnesium for the mixture $2.7CH_4 + 2O_2 + 5.8N_2$, tube bore diameter-38 mm and the projectile details for the model being: metal- magnesium, fins- 4, diameter- 29 mm, length- 71 mm, thickness- 3 mm with initial mass being 63.72 g and fill pressure 24 atm. The ablation initiation velocity as seen for the experiment is ~1600 m/s and that for the ablation model is 1462 m/s and the difference is ~11 %. The difference in the ablation initiation distance is ~2 m. In this case the slope of the velocity-distance curve is similar to that of the experimental data, indicating that the theoretical thrust-Mach profile is in relatively good agreement up to Mach 5.

The velocity-distance plot for run HS1022 is shown in Fig. 4.15. The material of the projectile in this particular run is magnesium, the projectile details for the model being: metal- magnesium, fins- 4, diameter- 29 mm, length- 71 mm, thickness- 3 mm with initial mass being 62.76 g and fill pressure 24 atm. The gaseous propellant mixture is $2.7CH_4 + 2O_2 + 5.8N_2$. It is observed that the difference in the ablation initiation velocities and the ablation initiation distance for the experiment and the ablation model is negligible. Indeed, the theoretical velocity-distance profile agreed well with experiment until the projectile velocity exceeded 97% CJ speed, at which point the experiment demonstrated greater thrust than predicted. This good agreement between theory and experiment indicates that the ablation model predicts similar thrust characteristics to experiment when the experimental thrust begins to deviate from theory at around 1460 m/s, which is Mach 4.0 in this propellant.

Velocity-distance profile for run HS678 with aluminum projectile, the projectile details for the model being: metal- aluminum, fins- 4, diameter- 29 mm, length- 71 mm, thickness- 3 mm with the initial mass being 77.41 g and fill pressure 33 atm, is as shown in Fig. 4.16. In this case the difference in the ablation initiation velocities for the experiment and the theoretical model is about 7 % since the initiation velocity for the experiment is ~1600 m/s and that for the ablation model is 1462 m/s; whereas the slope of the theoretical curve is nearly parallel to experiment. This indicates that once ablation begins, the predicted thrust is in reasonably good agreement for this experiment.

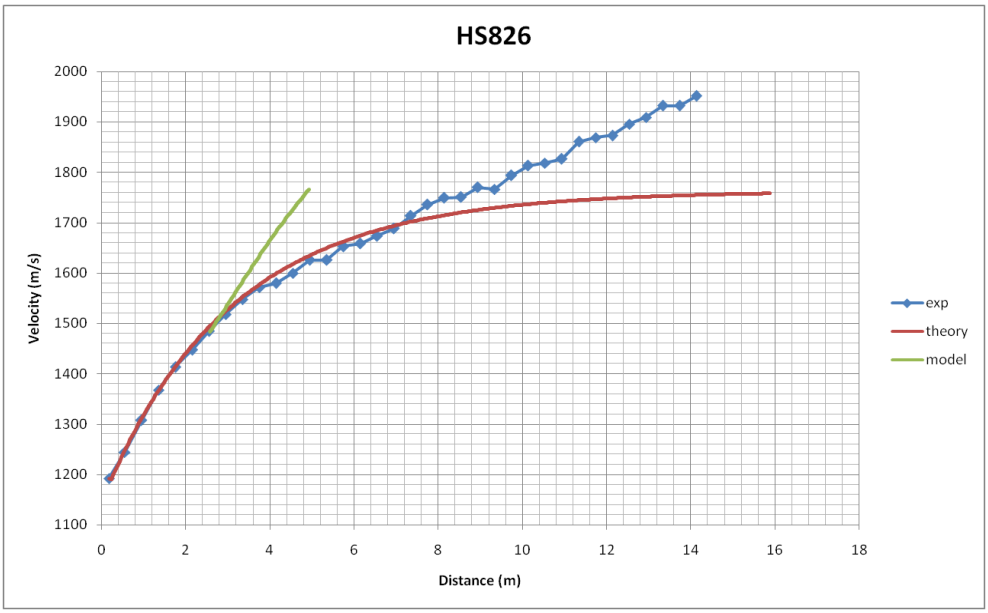

Fig. 4.13 HS826, UW, Al-alloy, 72.4 g, 25 atm

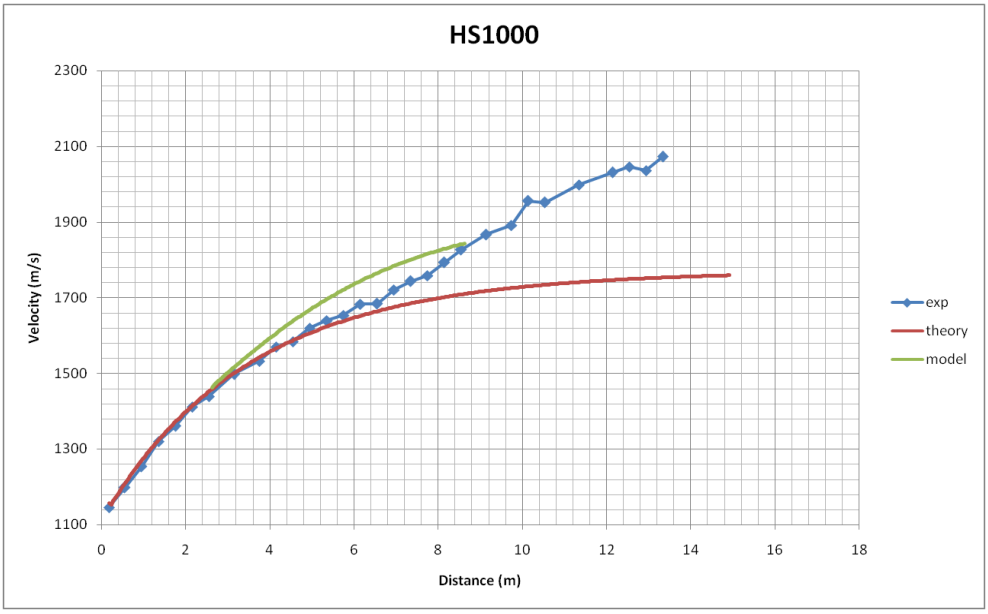

Fig. 4.14 HS1000, UW, Mg-alloy, 63.72 g, 24 atm

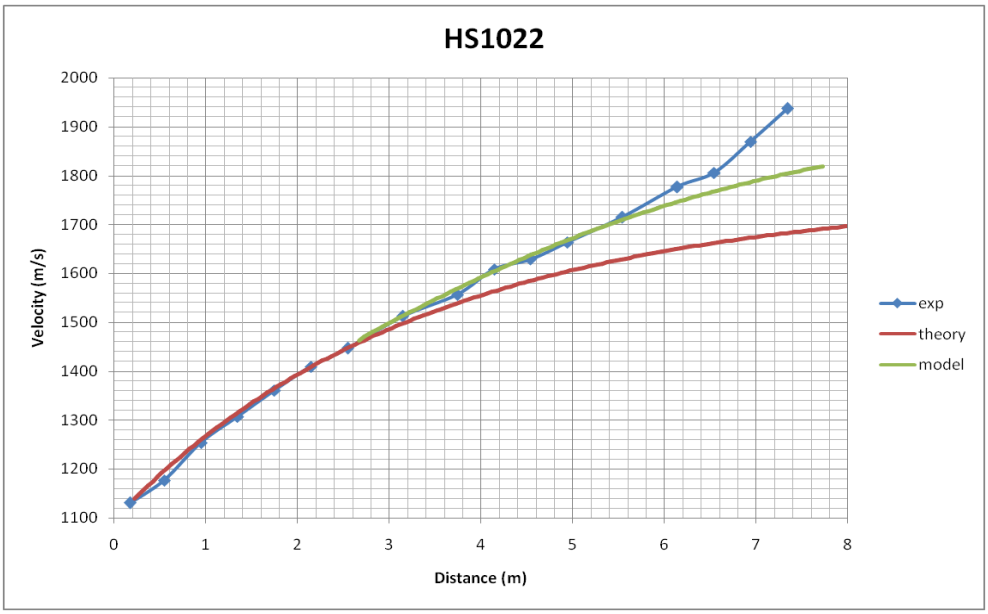

Fig. 4.15 HS1022, UW, Mg-alloy, 62.76 g, 24 atm

Fig. 4.16 HS678, UW, Al-alloy, 77.41 g, 33 atm

In the 38-mm-bore ram accelerator system, it is apparent that the ablation theoretical model predicts an earlier onset of ablation than is indicated by experiment. This indicates that the heat transfer coefficient and/or transient heat conduction models may need some revision to better predict experimental operating characteristics.

4.5.2 Velocity-distance profile for 25-m-bore ram accelerator

The velocity-distance profile for the 25-mm-bore ram accelerator with the projectile made of aluminum is as shown in Fig. 4.17. The propellant mixture is $2.8CH_4 + 2O_2 + 5.7N_2$ and tube bore diameter-25 mm with projectile details for the model being: metal-aluminum, fins- 4, throat diameter-19 mm, length- 47 mm, thickness- 2 mm. The projectile has an initial mass of 18.5 g and the fill pressure is 35 atm. It can be seen from this figure that the ablation initiation velocity for the experiment is ~1600 m/s and for the ablation model it is ~1462 m/s. Thus the difference between the ablation initiation velocities is ~8%. The ablation initiation distances differ by ~1.5 m. The slope of the theory curve compares well with experiment, indicating relatively good agreement in predicted thrust characteristics.

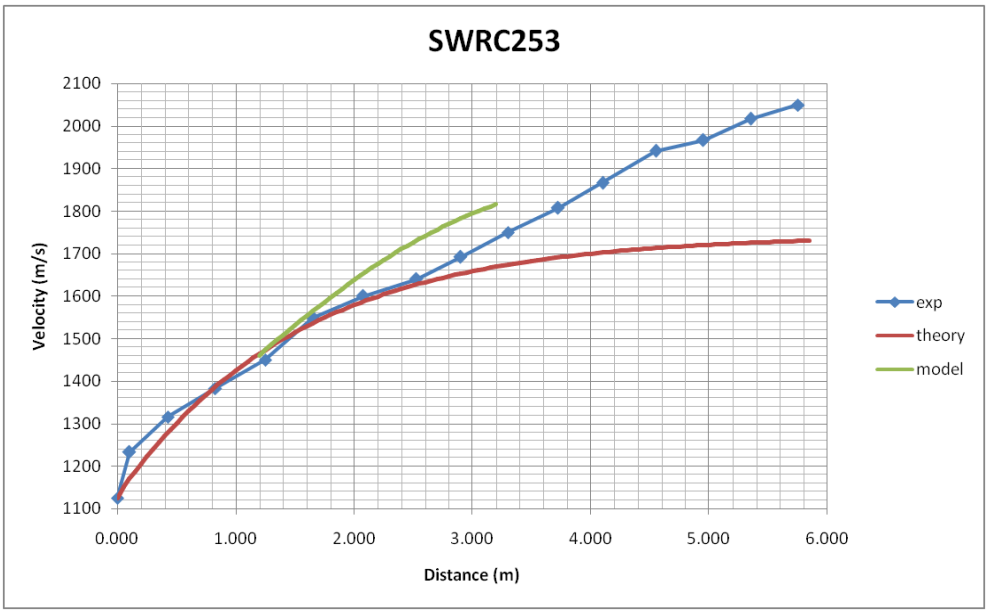

Fig. 4.17 SWRC25 3rd data set, SWR, Al-alloy, 18.5 g, 35 atm

4.5.3 Velocity-distance profile for 90-m-bore ram accelerator

The velocity-distance profile for the 90-mm-bore ram accelerator with the projectile made of aluminum is as shown in Fig. 4.18. The propellant mixture chemistry is $3CH_4 + 2O_2 + 9.7N_2$ and the projectile made of aluminum with 4 fins and the throat diameter of 68 mm with length being 362 mm and the wall thickness of 7 mm. The projectile has an initial mass of 1.3 kg and the fill pressure is 40 atm. In this data set, the experimental velocity-distance plot dips below the theory curve, however, it is not clear whether this is an artifact of the original time-distance data being curve fit and then differentiated for presentation purposes or if the experiment actually performed in this fashion. Curiously, the effects of the ablation model result in a decrease in thrust with respect to theory in this velocity range much like that experienced by the projectile. The ablation initiation velocity for the experiment is ~1600 m/s and that for the ablation model is 1512 m/s and the corresponding difference

being ~5%. The ablation initiation distances differ by 4 m. Thus the ablation model works to a reasonable extent for any of the analyzed bore diameters of the ram accelerator tube.

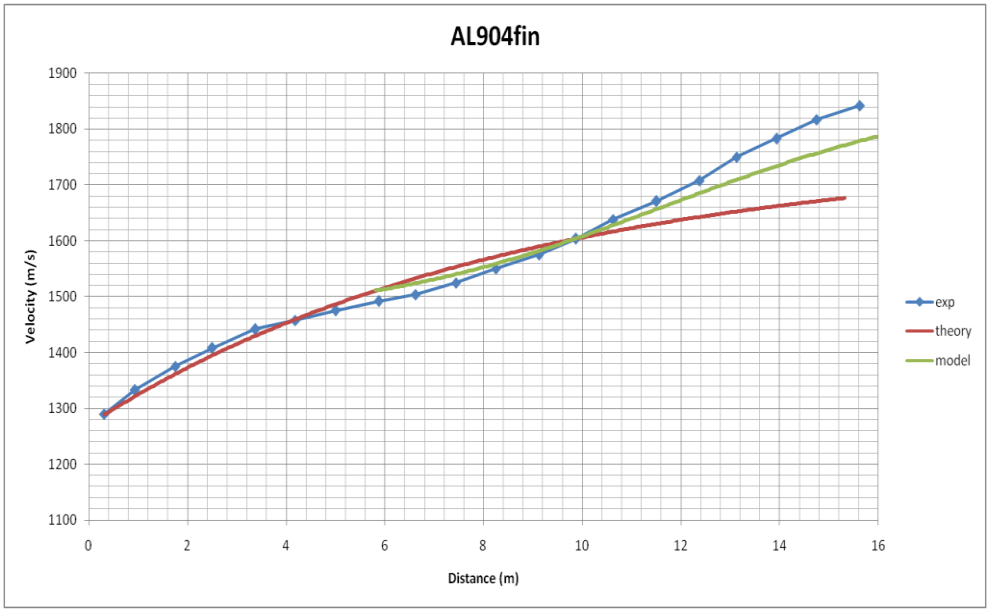

Fig. 4.18 Aluminum projectile 90 mm ram accelerator tube with 4 fins, ISL, 1.3 kg, 40 atm

4.6 Ablation and subsequent combustion initiation velocities

The predictions for ablation initiation velocity (reported in terms of fraction of V_{CJ}) and travel distance at which this occurs in the tube are listed for many experiments in Table 4.3. The experiments demonstrated signs of ablation at 90-95% of CJ speed in most cases, whereas the theory typically predicted the ablation initiation velocity to occur around 83-90% V_{CJ}. There was thus an average deviation of 6.4% between the theoretical and experimental ablation initiation velocities. This difference can be prominently seen in the scatter plot in Fig. 4.19 for the difference in initiation velocities (normalized to CJ speed) vs. the initiation distance. Since this constant offset is usually positive, it can be attributed, in part, to some shortcomings in the ablation model developed here and/or the data acquisition for the experimental runs.

The discrepancy between theory and experiment is also evident by the data plotted in Fig. 4.20, which show the ablation initiation velocity for the experiment and the ablation model vs. the CJ velocity for the respective propellant gas mixture for every run analyzed. In propellants with low CJ speeds (i.e., less than 1700 m/s), the difference is relatively small. This may be due to the corresponding low Mach of the CJ wave or, in the case of 90-mm-projectiles, the smaller surface-to-volume ratio of the projectiles.

Run #	Initiation velocity experiment (m/s)	Initiation velocity model (m/s)	% Vcj experiment	% Vcj model	Difference in % velocities	Initiation distance experiment (m)	Initiation distance model (m)	Difference in Initiation distance
HS675	1533	1462	90.08	85.89	0.042	5.10	4.45	0.65
HS678	1537	1462	90.19	85.79	0.044	3.55	3.40	0.15
HS679	1554	1462	91.19	85.79	0.054	3.95	3.25	0.70
HS687	1563	1512	90.08	87.14	0.029	5.80	4.65	1.15
HS688	1579	1462	91.63	84.85	0.068	4.87	3.37	1.50
HS689	1600	1462	94.06	85.94	0.081	4.94	2.62	2.32
HS690	1611	1462	92.64	84.07	0.086	6.14	4.32	1.82
HS706	1594	1516	93.71	89.12	0.046	8.54	7.09	1.45
HS750	1616	1468	92.25	83.79	0.085	6.32	3.12	3.20
HS753	1697	1479	96.75	84.31	0.124	9.27	3.12	6.15
HS755	1685	1462	96.72	83.93	0.128	7.32	3.07	4.25
HS762	1653	1469	93.71	83.28	0.104	5.17	2.17	3.00
HS826	1699	1519	96.70	86.45	0.102	7.22	2.77	4.45
HS835	1684	1462	100.00	86.82	0.132	11.92	4.82	7.10
HS843	1489	1462	88.11	86.51	0.016	3.00	2.60	0.40
HS997	1582	1464	91.82	84.96	0.069	4.97	2.87	2.10
HS999	1613	1467	92.17	83.83	0.083	5.32	2.72	2.60
HS1000	1598	1463	90.90	83.22	0.077	4.77	2.62	2.15
HS1001	1491	1463	85.20	83.60	0.016	3.12	2.72	0.40
HS1004	1532	1463	87.54	83.60	0.039	3.75	2.77	0.97
HS1008	1560	1465	89.14	83.71	0.054	5.02	3.12	1.90
HS1017	1569	1454	92.02	85.28	0.067	4.77	2.97	1.80
HS1019	1601	1463	91.70	83.79	0.079	4.97	2.72	2.25
HS1022	1512	1463	88.94	86.06	0.029	3.15	2.67	0.47
HS1077	1539	1462	87.74	83.35	0.044	2.15	1.77	0.37
SWRC251	1595	1465	93.06	85.47	0.076	2.55	1.35	1.20
SWRC252	1542	1437	93.06	86.72	0.063	2.90	1.65	1.25
SWRC253	1543	1460	89.19	84.39	0.048	1.70	1.20	0.50
SWRC254	1538	1460	90.47	85.88	0.046	1.50	1.00	0.50
AL903fin1	1616	1512	95.85	89.68	0.062	9.83	5.58	4.25
AL903fin2	1538	1512	96.43	94.79	0.016	10.20	8.45	1.75
AL904fin	1607	1512	95.88	90.21	0.057	9.96	5.81	4.15
AL905fin1	1612	1511	95.90	89.89	0.060	9.61	5.31	4.30
AL905fin2	1594	1512	94.82	89.95	0.049	8.91	5.26	3.65
Average	**1585**	**1474**	**92.34**	**85.94**	**0.064**	**5.66**	**3.45**	**2.20**
Std Dev	**54.8179**	**22.6655**	**3.2676**	**2.5937**	**0.0303**	**2.7382**	**1.6480**	**1.7306**

Table 4.3 Initiation velocities and distances

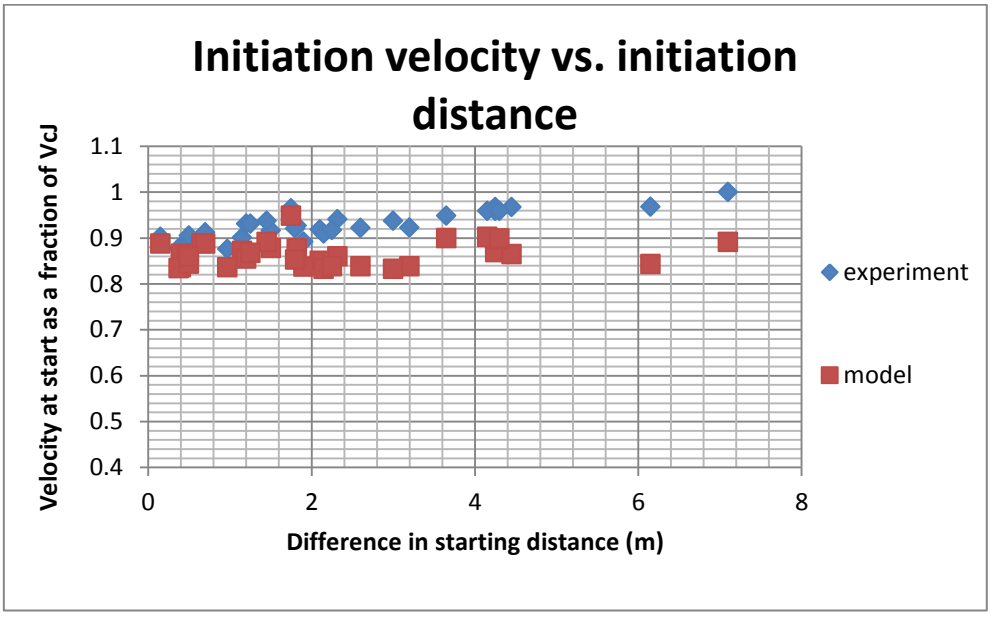

Fig. 4.19 Scatter plot for initiation velocity and distances

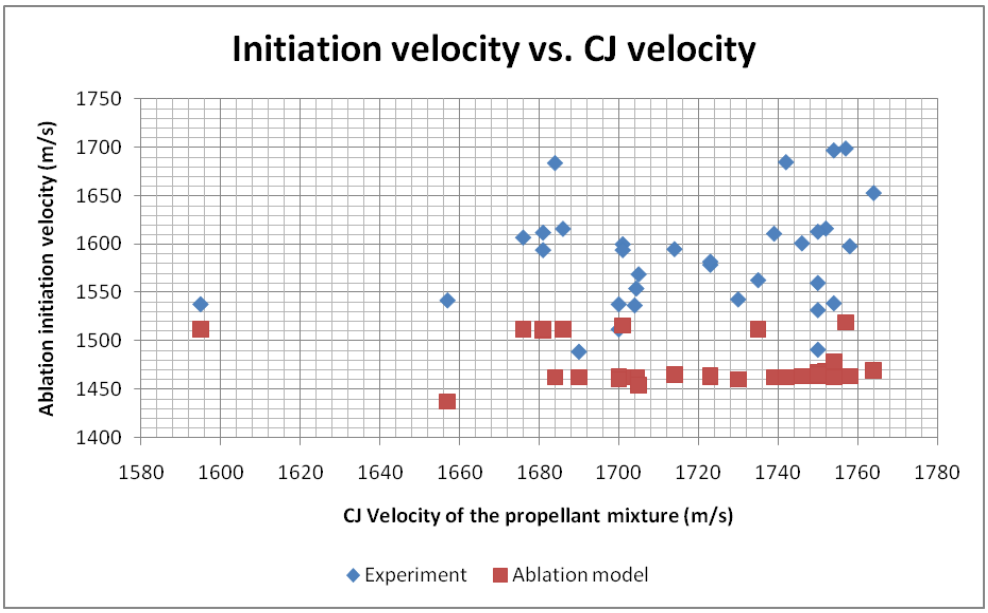

Fig. 4.20 Initiation velocity vs. CJ velocity of the gaseous mixture

Chapter 5 Discussion and future scope

The data from the various bore diameter ram accelerators were analyzed. These data were obtained from experiments using projectiles of various configurations and dimensions which were made of aluminum and magnesium. It was observed that the ablation initiation velocities for the experimental and theoretical ablation profiles were offset by 6.4% on an average. Also, this offset was always positive, or in other words the ablation initiation velocity from the experimental data was always greater than the ablation initiation velocity obtained from the theoretical ablation model. Since the experimental results too have some uncertainties, this offset might be insignificant if those uncertainties are accounted for.

In the data obtained from the 90-mm-bore ram accelerator, a small decrease in the thrust was observed right after the ablation initiation velocity for all runs analyzed which also matches with the experimental curve to some extent. The exact reason for the occurrence of this phenomenon, however was not further explored. Nevertheless, the predicted reduction of thrust over a small velocity regime indicates that the ablation model developed in this thesis can account for numerous changes in the flow parameters that occur during the ram shots. Effects of projectile surface-to-volume ratio predicted i.e., larger projectiles would have to achieve higher Mach numbers before enhanced thrust could be generated by metal added to flow supported by published data, can be seen in the 38-mm-bore and 90-mm-bore ram projectiles.

The projectiles of 25-mm-bore and 38-mm-bore did not show significant differences in Mach numbers before enhanced thrust was detected. This may be due to the fact that the dimensions of the projectile in the 38-mm-bore ram tube do not vary by a lot (10 mm difference in the throat diameters) from the 25-mm-bore projectiles. However, the projectiles from the 90-mm-bore and the 38-mm-bore have a difference of about 40 mm for their throat diameters. The slopes of the ablation model curves in most runs were similar to those of the experimental curve. This indicates that the thrust predicted by the ablation model was in good agreement with the experimental values.

The deviations seen in the ablation initiation velocities signify that the model needs to be refined before being applied in future studies. The heat coefficient calculated at each time step can be modified to match the fill pressure for a particular run. The exact projectile geometries can be taken into account and checked for their influence on the ablation initiation velocities. The method to account for the effect of including the nose-cone shocks on the pressure and temperature over the cylindrical part of the projectile and the fins can be developed which will give better numbers for the transport properties of the flow over the projectile thus affecting the ablation initiation velocities. Ultimately, a coupled CFD / heat transfer / ablation code (e.g., CTH or LS-Dyna) may be used for these studies.

Chapter 6 Conclusion

The ablation model developed in this thesis was successful in predicting the enhanced thrust experienced by projectiles operating above Mach 4 in the ram accelerator experiments. This supports the hypothesis that the enhanced thrust can, at least in part, be attributed to the ablation or melting of the projectile and its subsequent combustion with the propellant gas flow around the projectile. The ablation theory developed here predicts the Mach number at which the projectile will first experience the enhanced thrust. This predicted Mach number and the corresponding velocity-distance profile of individual ram accelerator experiments is close to that seen from the data from 25, 38, and 90-mm-bore ram accelerator facilities.

The prediction that larger projectiles will need to achieve greater Mach numbers before enhanced thrust can be generated is confirmed with the ablation model along with the previous supportive evidence from the experimental data as seen from the results of the ablation model applied to the 90-mm-bore and 38-mm-bore projectiles. This suggests that larger projectiles can withstand ablation to a greater degree without it introducing significant amounts of metal oxides in the exhaust.

The ablation phenomenon is seen for projectiles made of both aluminum and magnesium alloys. The enhanced thrust generated above Mach 5 was not be modeled here because the present ablation model was developed for the Mach range of 3-5, although the it can be extended to higher Mach numbers by using ram accelerator codes that do not enforce thermal choking on the equilibrium. Phenomena other than ablation that might account for the experimental characteristics observed at higher Mach numbers, such as mixed mode combustion on the projectile body, were not studied in this research effort, but should be at some point. The projectiles made of titanium alloys which have a melting temperature around 1800 K do not show the ablation phenomenon up until Mach 5 since the temperature around the projectile generated due to aerodynamic heating is around 1650 K.

Appendix A

A.1 MATLAB codes

A.1.1 Aerodynamic heating flow properties

```
function [x,iter]=newton(x0,f,fp)
% newton-raphson algorithm
N = 10000; eps = 1.e-10; % define max. no. iterations and error
maxval = 1000000000000.0; % define value for divergence
xx = x0;
while (N>0)
 xn = xx-f(xx)/fp(xx);
if abs(f(xn))<eps
 x=xn;iter=10001-N;
 return;
end;
if abs(f(xx))>maxval
 disp(['iterations = ',num2str(iter)]);
 error('Solution diverges');
 abort;
end;
 N = N - 1;
 xx = xn;
end;
error('No convergence');
abort;
%end function
```

```
clear all;close all;clc;
T1=300; % Define fill pressure and temperature
P1=40;
r=1.36;
A=(3476/8100)^(2*(r-1)/(r+1));
M1=5;
B=(1/M1)^(2*(r-1)/(r+1)).*(1+0.5*(r-1)*M1^2);
K=A.*B;
To1=T1.*(1+0.5*(r-1)*M1^2); % Calculate stagnation values
Po1=P1*(1+0.5*(r-1)*M1^2)^(r/(r-1));
f=@(x) 0.5*(r-1)*x^2-K*x^(2*(r-1)/(r+1))+1; %Newton's numerical method
fp=@(x) (r-1)*x-(2*(r-1)/(r+1)).*K*x^((2*(r-1)/(r+1))-1);
[x,iter]=newton(2,f,fp) % Solve for M2
T2=To1/(1+0.2*x^2);
P2=P1*(T2/T1)^3.77;
Pos=Po1*((1+(2*r/(r+1))*(x^2-1))^(-1/(r-1))*((r+1)*x^2/((r-1)*x^2+2))^(r/(r-1)));
Ms=((1+0.18*x^2)/(1.36*x^2-0.18))^0.5 %Flow properties aft of the normal shock
Ps=P2*(1+1.15*(x^2-1))
To2=To1;
Ts=T2*(1+(2*r*(r-1)/(r+1)^2)*((x^2+1)/x^2)*(x^2-1))
M2=x
```

Published with MATLAB® R2014a

A.1.2 Bartz heat coefficient

```
clear all;close all;clc
prompt = {'Enter value of To:','Enter value of Tw:','Enter value of Ts:','Enter value of
Ms:','Enter value of Dt:','Enter value of mu:','Enter value of Cp:'...
    ,'Enter value of Pr:','Enter value of Ps:','Enter value of r:'};
dlg_title = 'Input';
num_lines = 1;
%defaultans = {'20','hsv'};
answer = inputdlg(prompt,dlg_title,num_lines); %Input all required variables
To=str2double(answer{1,1});
Tw=str2double(answer{2,1});
Ts=str2double(answer{3,1});
M=str2double(answer{4,1});
Dt=str2double(answer{5,1})/1000; %converting to correct units
u=str2double(answer{6,1})*10^-7;
Cp=str2double(answer{7,1})*1000;
Pr=str2double(answer{8,1});
Ps=str2double(answer{9,1})*101325;
r=str2double(answer{10,1});
Ps1=Ps/101325;
Cv=Cp/r;
a=(r*(Cp-Cv)*Ts)^0.5; %sonic velocity
C=(a/r)*(0.5*(r+1))^((r+1)/(2*(r-1)));
e=(0.5*(Tw/To)*(1+0.5*(r-1).*M^2)+0.5)^(-0.68)*(1+0.5*(r-1).*M^2)^(-0.12);
A=(0.026/Dt^0.2);
B=((u^0.2*Cp)/Pr^0.6);
D=(Ps/C)^0.8;
hB=A*B*D*e %Bartz equation
```

Published with MATLAB® R2014a

A.1.3 Velocity – distance profile

```
%  forward Euler method
clear all; close all; clc;
T1=300;
u0 = 1459; % Velocity at which metal is added
v0= 1145; %initial velocity

P = 2800000; %Fill pressue
A = .001134; %Area of bore
m = 0.0743; %mass of projectile
PA_m = P*A/m;

% Plotting profile with metal addition
h=0.001;
x = 2.582:h:10;
ustar = zeros(size(x));
a=363; % scale of output is strongly dependent on a
ustar(1) = u0;
```

```
for i=1:(length(x)-1)
f_of_u =-(4.503*(ustar(i)/a)^2)+(40.59*(ustar(i)/a))-86.50 ; %Model from thrust profile
PA_mU = PA_m/ustar(i);
du_dx = f_of_u*PA_mU;
ustar(i+1) = ustar(i) + h*du_dx;
end
%Plotting profile without the metal addition
k=0.001;
y = 0:k:10;
vstar = zeros(size(y));
a1=363; % scale of output is strongly dependent on a
vstar(1) = v0;
for jj=1:(length(y)-1)
fu = (0.052*(vstar(jj)/a1)^3)-(1.344*(vstar(jj)/a1)^2)+(5.512*(vstar(jj)/a1))-1.020 ;% Model
from thrust profile
PAmU = PA_m/vstar(jj);
dv_dy = fu*PAmU;
vstar(jj+1) = vstar(jj) + k*dv_dy;
end
plot(x,ustar,y,vstar,'LineWidth',2);
xlabel('Distance (m)');
ylabel('Velocity (m/s)');
title('Velocity-Distance plot');
grid on;
grid minor;
```

Published with MATLAB® R2014a

A.2 Modeling Procedure step 1

Modeling procedure step 4.1: NASA CEA-hp calculation with liquid metal at stagnation temperature and the mixture components at stagnation temperature at Mach 4.3056 for 38mm bore with aluminum projectile:

```
 ******************************************************************************

        NASA-GLENN CHEMICAL EQUILIBRIUM PROGRAM CEA2, MAY 21, 2004
                  BY  BONNIE MCBRIDE AND SANFORD GORDON
     REFS: NASA RP-1311, PART I, 1994 AND NASA RP-1311, PART II, 1996

 ******************************************************************************


problem
    hp
p,bar=657.74,
t,k=3800 react
  fuel=AL(L) moles=0.1433 t,k=1366
  oxid=O2 moles=0.4453 t,k=1366
  fuel=CH4 moles=0.5566 t,k=1366
  name=N2 moles=1.2245 t,k=1366



        THERMODYNAMIC EQUILIBRIUM COMBUSTION PROPERTIES AT ASSIGNED
```

```
                                   PRESSURES

 CASE =

             REACTANT                          MOLES          ENERGY     TEMP
                                                             KJ/KG-MOL      K
 FUEL        AL(L)                          0.1433000       42574.276  1366.000
 OXIDANT     O2                             0.4453000       35738.957  1366.000
 FUEL        CH4                            0.5566000       -6341.967  1366.000
 NAME        N2                             1.2245000       33764.699  1366.000

 O/F=     0.30254  %FUEL= 76.773065  R,EQ.RATIO= 2.741242  PHI,EQ.RATIO= 2.741242


 THERMODYNAMIC PROPERTIES

 P, BAR             657.74
 T, K              2720.31
 RHO, KG/CU M     6.1714 1
 H, KG/KG           975.28
 U, KG/KG          -90.506
 G, KG/KG         -25772.8
 S, KJ/(KG)(K)      9.8327

 M, (1/n)           21.222
 MW, MOL WT         20.710
 (dLV/dLP)t       -1.00261
 (dLV/dLT)p         1.0121
 Cp, KJ/(KG)(K)     2.0399
 GAMMAs             1.2409
 SON VEL,M/SEC      1150.0

 MOLE FRACTIONS
 ALOH               0.00007
 AL(OH)2            0.00001
 AL(OH)3            0.00002
 CH3                0.00001
 CH4                0.00014
 *CO                0.18373
 *CO2               0.00308
 *H                 0.00137
 HCN                0.00077
 HCO                0.00002
 HNC                0.00010
 HNCO               0.00002
 *H2                0.33508
 HCHO,formaldehy    0.00002
 H2O                0.03809
 NH2                0.00001
 NH3                0.00071
 *N2                0.41256
 *OH                0.00004
 AL2O3(L)           0.02414


*THERMODYNAMIC PROPERTIES FITTED TO 20000.K
```

Fig. A.1 NASA CEA hp calculation output for liquid metal

The adiabatic flame temperature from the above output file is determined to be T = 2720.31 K.

NASA CEA ‘hp’ calculation with gaseous metal at room temperature and the mixture components at stagnation temperature at Mach 4.3056 for 38mm bore with Aluminum projectile:

```
******************************************************************************

        NASA-GLENN CHEMICAL EQUILIBRIUM PROGRAM CEA2, MAY 21, 2004
                  BY  BONNIE MCBRIDE AND SANFORD GORDON
     REFS: NASA RP-1311, PART I, 1994 AND NASA RP-1311, PART II, 1996

******************************************************************************



problem
    hp
p,bar=657.74,
t,k=3800 react
  fuel=AL    moles=0.1433    t,k=298
  oxid=O2    moles=0.4453    t,k=1366
  fuel=CH4   moles=0.5566    t,k=1366
  name=N2 moles=1.2245 t,k=1366

        THERMODYNAMIC EQUILIBRIUM COMBUSTION PROPERTIES AT ASSIGNED

                                PRESSURES



CASE =

            REACTANT                        MOLES          ENERGY      TEMP
                                                          KJ/KG-MOL       K
FUEL        AL                          0.1433000      329996.791   298.000
OXIDANT     O2                          0.4453000       35738.957  1366.000
FUEL        CH4                         0.5566000       -6341.967  1366.000
NAME        N2                          1.2245000       33764.699  1366.000

O/F=     0.30254  %FUEL= 76.773065  R,EQ.RATIO= 2.741242  PHI,EQ.RATIO= 2.741242

THERMODYNAMIC PROPERTIES

P, BAR             657.74
T, K              3039.46
RHO, KG/CU M     5.5129 1
H, KG/KG           1646.66
U, KJ/KG            453.56
G, KJ/KG           -28948.3
S, KJ/(KG)(K)      10.0659

M, (1/n)            21.181
MW, MOL WT          20.676
(dLV/dLP)t        -1.00298
(dLV/dLT)p          1.0256
Cp, KJ/(KG)(K)      2.1872
GAMMAs              1.2282
SON VEL,M/SEC       1210.5


MOLE FRACTIONS

ALH               0.00001
ALOH              0.00050
AL(OH)2           0.00003
AL(OH)3           0.00003
CH3               0.00001
CH4               0.00005
*CO               0.18372
*CO2              0.00282
*H                0.00396
HCN               0.00076
HCO               0.00004
HNC               0.00014
```

```
HNCO              0.00002
*H2               0.33302
HCHO,formaldehy   0.00002
H2O               0.03828
NH2               0.00003
NH3               0.00055
*NO               0.00002
*N2               0.41193
*OH               0.00017
AL2O3(L)          0.02386


*THERMODYNAMIC PROPERTIES FITTED TO 20000.K
```

Fig. A.2 NASA CEA hp calculation output for gaseous metal

The adiabatic flame temperature from the above output can be seen to be T = 3039.46 K.

Thus, the amount of metal converted to gaseous state with the available energy in the flow would be less than the total molten metal quantity. These metallic gas moles can be estimated by reducing the input for the metal moles until the adiabatic flame temperature is within a range of the adiabatic flame temperature from the previous output. This is done as shown below:

```
 ******************************************************************************

        NASA-GLENN CHEMICAL EQUILIBRIUM PROGRAM CEA2, MAY 21, 2004
                    BY  BONNIE MCBRIDE AND SANFORD GORDON
     REFS: NASA RP-1311, PART I, 1994 AND NASA RP-1311, PART II, 1996

 ******************************************************************************


 problem
     hp
 p,bar=657.74,
 t,k=3800 react
   fuel=AL moles=0.080 t,k=298
   oxid=O2 moles=0.4453 t,k=1366
   fuel=CH4 moles=0.5566 t,k=1366
   name=N2 moles=1.2245 t,k=1366


         THERMODYNAMIC EQUILIBRIUM COMBUSTION PROPERTIES AT ASSIGNED

                                    PRESSURES

 CASE =

             REACTANT                        MOLES          ENERGY      TEMP
                                                          KJ/KG-MOL       K
 FUEL        AL                          0.0800000      329996.791   298.000
 OXIDANT     O2                          0.4453000       35738.957  1366.000
 FUEL        CH4                         0.5566000       -6341.967  1366.000
 NAME        N2                          1.2245000       33764.699  1366.000

 O/F=     0.31392  %FUEL= 76.107898  R,EQ.RATIO= 2.634628  PHI,EQ.RATIO= 2.634628

 THERMODYNAMIC PROPERTIES

 P, BAR             657.74
 T, K              2727.73
 RHO, KG/CU M     5.9790 1
```

```
H, KJ/KG           1343.57
U, KJ/KG            243.49
G, KJ/KG          -26150.3
S, KJ/(KG)(K)      10.0794

M, (1/n)            20.616
MW, MOL WT          20.336
(dLV/dLP)t         -1.00176
(dLV/dLT)p           1.0104
Cp, KJ/(KG)(K)       2.0407
GAMMAs               1.2500
SON VEL,M/SEC       1172.6


MOLE FRACTIONS

ALOH              0.00005
AL(OH)2           0.00001
AL(OH)3           0.00004
CH4               0.00006
*CO               0.18336
*CO2              0.00588
*H                0.00136
HCN               0.00038
HCO               0.00002
HNC               0.00005
HNCO              0.00002
*H2               0.30997
HCHO,formaldehy   0.00002
H2O               0.06746
NH2               0.00001
NH3               0.00063
*NO               0.00001
*N2               0.41699
*OH               0.00009
AL2O3(L)          0.01359

 * THERMODYNAMIC PROPERTIES FITTED TO 20000.K
```

Fig. A.3 NASA CEA adjusted liquid metal amount output file

The adiabatic flame temperature as seen in the above output file is T = 2727.73 K (this is within 25K of the initial adiabatic flame temperature of 2720.31 K). The number of gaseous moles of Aluminum thus is 0.080 moles as compared to the 0.1433 moles of Al in liquid state.

A.3 Modeling Procedure Step 2

Details for geometry, meshing, analysis and load setting for the cylindrical part of the projectile and the projectile fins used on ANSYS are described below. The cylindrical part is designed as a 2D object while a full 3D version of the fin is analyzed.

Projectile Cylindrical Aftbody:

Symmetry

Object Name	*Symmetry*
State	Fully Defined
Graphical Expansion 1 (Beta)	
Num Repeat	37
Type	2D AxiSymmetric
Δθ	10. °
Coordinate System	Global Coordinate System

Tab. A.1 ANSYS 2D symmetric design specifications

Mesh

Object Name	*Mesh*
State	Solved
Display	
Display Style	Body Color
Defaults	
Physics Preference	CFD
Solver Preference	Fluent
Relevance	0
Export Format	Standard
Sizing	
Use Advanced Size Function	Off
Relevance Center	Coarse
Element Size	Default
Initial Size Seed	Active Assembly
Smoothing	Medium
Transition	Slow
Span Angle Center	Fine
Minimum Edge Length	1.626e-003 m
Inflation	
Use Automatic Inflation	None

Inflation Option	Smooth Transition
Transition Ratio	0.272
Maximum Layers	2
Growth Rate	1.2
Inflation Algorithm	Pre
View Advanced Options	Yes
Collision Avoidance	Layer Compression
Fix First Layer	No
Gap Factor	0.5
Maximum Height over Base	1
Growth Rate Type	Geometric
Maximum Angle	140.0 °
Fillet Ratio	1
Use Post Smoothing	Yes
Smoothing Iterations	5
Assembly Meshing	
Method	None
Patch Conforming Options	
Triangle Surface Mesher	Program Controlled
Patch Independent Options	
Topology Checking	Yes
Advanced	
Number of CPUs for Parallel Part Meshing	Program Controlled
Shape Checking	CFD
Element Midside Nodes	Dropped
Straight Sided Elements	
Number of Retries	Default (0)
Extra Retries For Assembly	No
Rigid Body Behavior	Dimensionally Reduced
Mesh Morphing	Disabled
Defeaturing	
Use Sheet Thickness for Pinch	No
Pinch Tolerance	Please Define
Generate Pinch on Refresh	No

Sheet Loop Removal	No
Automatic Mesh Based Defeaturing	On
Defeaturing Tolerance	Default
Statistics	
Nodes	6552
Elements	6390
Mesh Metric	None

Tab. A.2 ANSYS cylindrical body mesh specifications

Mesh Controls

Object Name	*Face Meshing*	*Edge Sizing*	*Edge Sizing 2*	*Edge Sizing 3*
State	Fully Defined			
Scope				
Scoping Method	Geometry Selection			
Geometry	1 Face	2 Edges	1 Edge	
Definition				
Suppressed	No			
Mapped Mesh	Yes			
Method	Quadrilaterals			
Constrain Boundary	No			
Type		Number of Divisions		
Number of Divisions		71	90	
Behavior		Hard		
Bias Type		No Bias		
Advanced				
Specified Sides	No Selection			
Specified Corners	No Selection			
Specified Ends	No Selection			

Tab. A.3 ANSYS cylindrical body mesh control settings

Transient thermal analysis settings

Object Name	*Analysis Settings*
State	Fully Defined
Step Controls	
Number Of Steps	1.
Current Step Number	1.
Step End Time	1.e-003 s
Auto Time Stepping	On
Define By	Time
Initial Time Step	1.e-004 s
Minimum Time Step	1.e-004 s
Maximum Time Step	1.e-004 s
Time Integration	On
Solver Controls	
Solver Type	Program Controlled
Radiosity Controls	
Radiosity Solver	Program Controlled
Flux Convergence	1.e-004
Maximum Iteration	1000.
Solver Tolerance	0.1 W/m²
Over Relaxation	0.1
View Factor Method	Hidden
Number of Zones	200.
Axisymmetry Divisions	20.
Nonlinear Controls	
Heat Convergence	Program Controlled
Temperature Convergence	Program Controlled
Line Search	Program Controlled
Nonlinear Formulation	Program Controlled
Output Controls	
Calculate Thermal Flux	Yes
General Miscellaneous	No

Store Results At	All Time Points
Cache Results in Memory (Beta)	Never
Analysis Data Management	
Solver Files Directory	U:\thesis_hollow_v2_files\dp0\SYS\MECH\
Future Analysis	None
Scratch Solver Files Directory	
Save MAPDL db	No
Delete Unneeded Files	Yes
Nonlinear Solution	Yes
Solver Units	Active System
Solver Unit System	Mks

Tab. A.4 ANSYS transient thermal analysis settings

Load

Object Name	*Convection*	*Heat Flow*
State	Fully Defined	
Scope		
Scoping Method	Geometry Selection	
Geometry	1 Edge	
Definition		
ID (Beta)	38	78
Type	Convection	Perfectly Insulated
Film Coefficient	2.6221e+006 W/m²·K (step applied)	
Ambient Temperature	1504. K (step applied)	
Convection Matrix	Program Controlled	
Suppressed	No	
Define As		Perfect Insulation
Magnitude		0. W

Tab. A.5 ANSYS thermal load specifications- cylindrical body

Projectile Fins:

Mesh

Object Name	*Mesh*
State	Solved
Display	
Display Style	Body Color
Defaults	
Physics Preference	Mechanical
Relevance	0
Sizing	
Use Advanced Size Function	On: Curvature
Enable Size Field (Beta)	No
Relevance Center	Coarse
Initial Size Seed	Active Assembly
Smoothing	Medium
Transition	Fast
Span Angle Center	Coarse
Curvature Normal Angle	Default (30.0 °)
Min Size	Default (2.1084e-004 m)
Max Face Size	Default (1.0542e-003 m)
Max Size	Default (1.0542e-003 m)
Growth Rate	Default
Minimum Edge Length	7.487e-004 m
Inflation	
Use Automatic Inflation	None
Inflation Option	Smooth Transition
Transition Ratio	0.272
Maximum Layers	5
Growth Rate	1.2
Inflation Algorithm	Pre
View Advanced Options	No
Patch Conforming Options	

Triangle Surface Mesher	Program Controlled
Patch Independent Options	
Topology Checking	No
Advanced	
Number of CPUs for Parallel Part Meshing	Program Controlled
Shape Checking	Standard Mechanical
Element Midside Nodes	Program Controlled
Straight Sided Elements	No
Number of Retries	Default (4)
Extra Retries For Assembly	Yes
Rigid Body Behavior	Dimensionally Reduced
Mesh Morphing	Disabled
Defeaturing	
Pinch Tolerance	Default (1.8975e-004 m)
Generate Pinch on Refresh	No
Sheet Loop Removal	No
Automatic Mesh Based Defeaturing	On
Defeaturing Tolerance	Default (1.5813e-004 m)
Statistics	
Nodes	14167
Elements	2700
Mesh Metric	None

Tab. A.6 ANSYS projectile fins mesh specifications

Mesh Controls

Object Name	*Edge Sizing*	*Edge Sizing 2*	*Edge Sizing 3*
State	Fully Defined		
Scope			
Scoping Method	Geometry Selection		
Geometry	1 Edge		
Definition			
Suppressed	No		

Type	Number of Divisions	
Number of Divisions	3	30
Behavior	Hard	
Bias Type	No Bias	

Tab. A.7 ANSYS projectile fins mesh conrtol settings

Analysis settings

Object Name	*Analysis Settings*
State	Fully Defined
Step Controls	
Number Of Steps	1.
Current Step Number	1.
Step End Time	1.e-003 s
Auto Time Stepping	On
Define By	Time
Initial Time Step	1.e-004 s
Minimum Time Step	1.e-004 s
Maximum Time Step	1.e-004 s
Time Integration	On
Solver Controls	
Solver Type	Program Controlled
Radiosity Controls	
Radiosity Solver	Program Controlled
Flux Convergence	1.e-004
Maximum Iteration	1000.
Solver Tolerance	0.1 W/m²
Over Relaxation	0.1
Hemicube Resolution	10.
Nonlinear Controls	
Heat Convergence	Program Controlled
Temperature Convergence	Program Controlled
Line Search	Program Controlled

Nonlinear Formulation	Program Controlled
Output Controls	
Calculate Thermal Flux	Yes
General Miscellaneous	No
Store Results At	All Time Points
Cache Results in Memory (Beta)	Never
Analysis Data Management	
Solver Files Directory	U:\fins_v1_files\dp0\SYS\MECH\
Future Analysis	None
Scratch Solver Files Directory	
Save MAPDL db	No
Delete Unneeded Files	Yes
Nonlinear Solution	Yes
Solver Units	Active System
Solver Unit System	mks

Tab. A.8 ANSYS analysis settings for projectile fins

Loads

Object Name	*Heat Flow*	*Convection*
State	Fully Defined	
Scope		
Scoping Method	Geometry Selection	
Geometry	4 Faces	2 Faces
Definition		
ID (Beta)	80	82
Type	Perfectly Insulated	Convection
Define As	Perfect Insulation	
Magnitude	0. W	
Suppressed	No	
Film Coefficient		2.864e+006 W/m²·K (step applied)
Ambient		1650. K (step applied)

Temperature		
Convection Matrix		Program Controlled

Tab. A.9 ANSYS projectile fins thermal loading specifications

A.4 Output file for the modeling procedure 4.3

```
*****************************************************************************

        NASA-GLENN CHEMICAL EQUILIBRIUM PROGRAM CEA2, MAY 21, 2004
                    BY  BONNIE MCBRIDE AND SANFORD GORDON
     REFS: NASA RP-1311, PART I, 1994 AND NASA RP-1311, PART II, 1996

*****************************************************************************


#                                SAMPLE PROBLEMS

!  TCRA input

reac  oxid O2  moles= 0.2783  t(k)=298.15
      fuel CH4 moles= 0.3478   t(k)=298.15
        name N2 moles= 0.7653  t(k)=298.15
      !fuel AL moles= 0.1395  t(k)=298.15
prob  tcramac case=61  t=298  pbar=30
output  short transport
end


                    DETONATION PROPERTIES OF AN IDEAL REACTING GAS
CASE = 61

            REACTANT                          MOLES         ENERGY      TEMP
                                                          KJ/KG-MOL         K
OXIDANT     O2                             0.2783000          0.000    298.150
FUEL        CH4                            0.3478000     -74600.000    298.150
NAME        N2                             0.7653000          0.000    298.150

O/F=    0.32960  %FUEL= 75.210464  R,EQ.RATIO= 2.499461  PHI,EQ.RATIO= 2.499461

UNBURNED GAS

P1, BAR           30.0000
T1, K              298.00
H1, KJ/KG         -722.31
M1, (1/n)          25.818
GAMMA1             1.3695
SON VEL1,M/SEC      362.5


 BURNED GAS

 P, BAR             443.89
 T, K              1967.16
 RHO, KG/CU M    5.4013 1
 H, KJ/KG           322.82
 U, KJ/KG           -498.99
 G, KJ/KG          -19183.7
 S, KJ/(KG)(K)      9.9161

 M, (1/n)           19.902
 (dLV/dLP)t       -1.00298
 (dLV/dLT)p         1.0164
 Cp, KJ/(KG)(K)     1.9408
 GAMMAs             1.2811
 SON VEL,M/SEC      1026.1

 TRANSPORT PROPERTIES (GASES ONLY)
   CONDUCTIVITY IN UNITS OF MILLIWATTS/(CM)(K)

 VISC,MILLIPOISE   0.65641

  WITH EQUILIBRIUM REACTIONS

 Cp, KJ/(KG)(K)     1.9408
 CONDUCTIVITY       2.2495
 PRANDTL NUMBER     0.5663

  WITH FROZEN REACTIONS

 Cp, KJ/(KG)(K)     1.8832
 CONDUCTIVITY       2.1928
 PRANDTL NUMBER     0.5637

 DETONATION PARAMETERS

 P/P1               14.796
 T/T1                6.601
 M/M1               0.7709
 RHO/RHO1           1.7279
 DET MACH NUMBER    4.8902
 DET VEL,M/SEC      1772.9
```

```
MOLE FRACTIONS

CH4                0.00049
*CO                0.17758
*CO2               0.01444
*H                 0.00003
HCN                0.00015
HNC                0.00001
HNCO               0.00002
*H2                0.28103
HCHO,formaldehy    0.00001
H2O                0.10188
NH3                0.00092
*N2                0.42345

 * THERMODYNAMIC PROPERTIES FITTED TO 20000.K
```

Fig. A.4 Output file for 4.3

Appendix B

B.1 Details of runs analyzed

Run #	Metal	Mass (g)	O2 (moles)	CH4 (moles)	N2 (moles)	P fill (atm)
HS674	AL	75.74	2	2.7	5.8	24.8
HS675	AL	83.8	2	2.7	5.8	26.1
HS678	AL	77.41	2	2.7	5.8	33.3
HS679	AL	79.4	2	2.7	5.8	35
HS687	Mg	66.27	2	2.7	5.8	20.73
HS688	AL	67.25	2	2.7	5.8	22.09
HS689	Mg	66.38	2	2.7	5.8	23.4
HS690	AL	85.2	2	2.7	5.8	22.09
HS706	Mg	64.8	2	2.9	5.6	21.77
HS727	AL	80.21	2	2.7	5.8	20.75
HS750	Mg	66.32	2	2.7	5.8	20.44
HS751	AL	71	2	2.7	5.8	21.43
HS752	AL	76.62	2	2.7	5.8	23.4
HS753	Mg	67.06	2	2.7	5.8	21.09
HS754	AL	77.86	2	3	5.5	24.15
HS755	AL	77	2	3	5.5	33.34
HS762	Mg	73.68	2	2.7	5.64	33.34
HS852	AL	72.7	2	2.5	5.5	30.28
HS826	AL	72.4	2	2.7	5.6	30.75
HS835	AL	88.4	2	2.6	5.1	23.13
HS836	AL	58.06	2	2.7	5.83	14.62
HS843	Mg	64.11	2	2.7	5.8	26.53
HS997	Mg	63.3	2	2.86	5.76	23.81
HS999	Mg	64.02	2	2.8	5.66	23.95
HS1000	Mg	63.72	2	2.8	5.5	23.95
HS1001	Mg	63.44	2	2.8	5	23.95
HS1004	Mg	64.31	2	2.8	5.3	24.02
HS1008	Mg	64	2	2.8	6	24.02
HS1017	Mg	64.54	2	2.8	5	24.02
HS1019	Mg	62.29	2	2.8	5.4	23.81
HS1022	Mg	62.76	2	2.8	5	24.02
HS1077	AL	76.71	2	2.8	6	30.55
SWRC251	AL	22.5	2	2.8	5.7	35
SWRC252	AL	22.5	2	2.8	5.7	25
SWRC253	AL	18.5	2	2.8	5.7	35
SWRC254	AL	18.5	2	2.8	5.7	35
AL903fin1	AL	1308	2	3.15	10.05	40
AL903fin2	AL	1253	2	3.25	9.8	40

AL904fin	AL	1332	2	2.95	9.9	40
AL905fin1	AL	1337	2	2.95	9.9	40
AL905fin2	AL	1337	2	3	9.7	40

Tab. B.1 Details of runs analyzed

B.2 Initiation velocities for various configurations

Bore Diameter (mm)	Initiation Velocity (m/s)
38 Aluminum	1462
38 Magnesium	1462
25 Aluminum	1462
90 Aluminum	1512

Tab. B.2 Initiation velocites for various ram configurations

B.3 Data comparison

The comparison between experimental and theoretical ablation curves for the runs analyzed:

Fig. B.1 HS 675, UW, Al-alloy, 83.8 g, 26 atm

Fig. B.2 HS678, UW, Al-alloy, 77.41 g, 33 atm

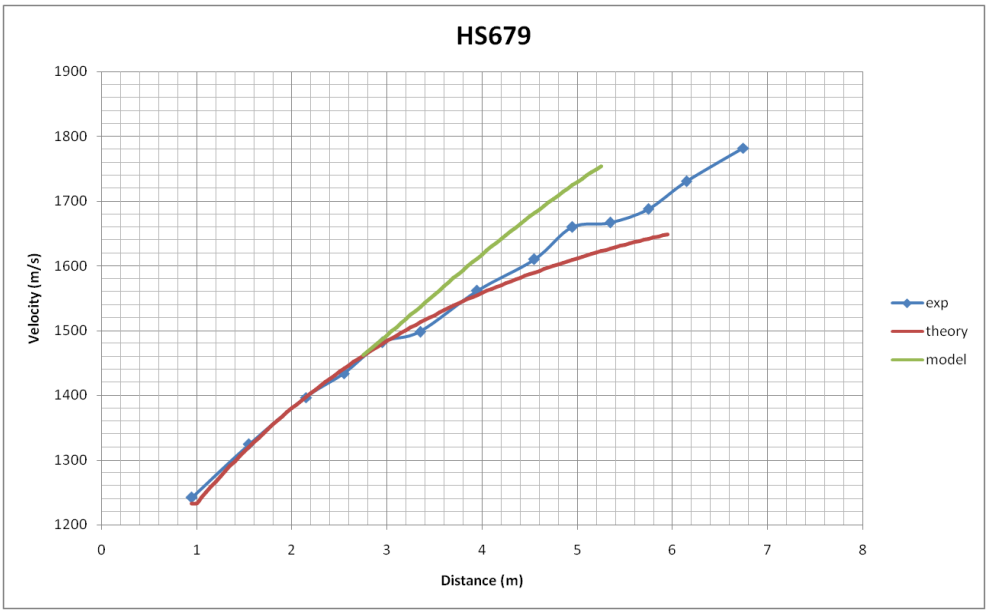

Fig. B.3 HS679, UW, Al-alloy, 79.4 g, 35 atm

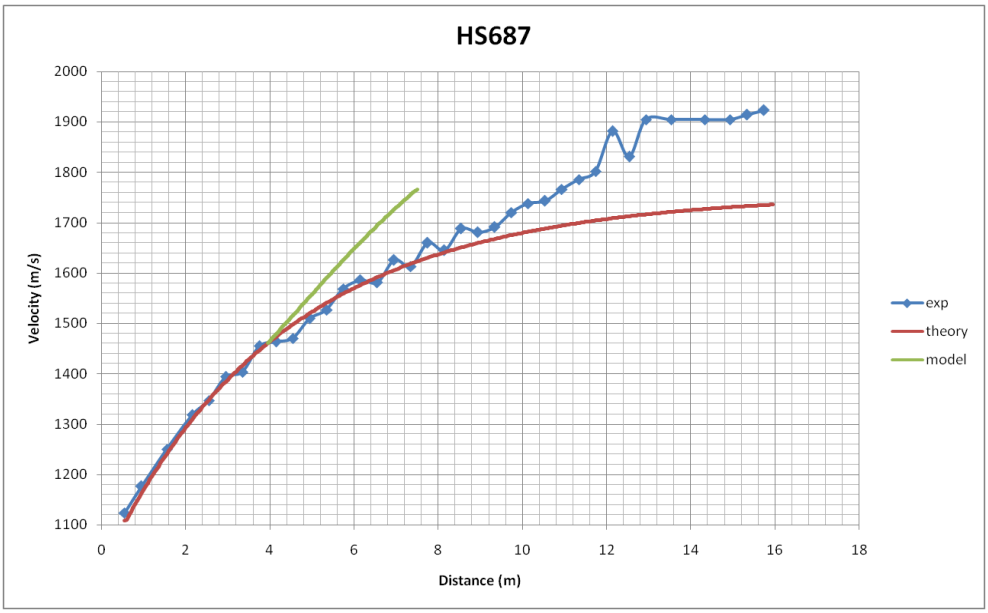

Fig. B.4 HS687, UW, Mg-alloy, 66.27 g, 20 atm

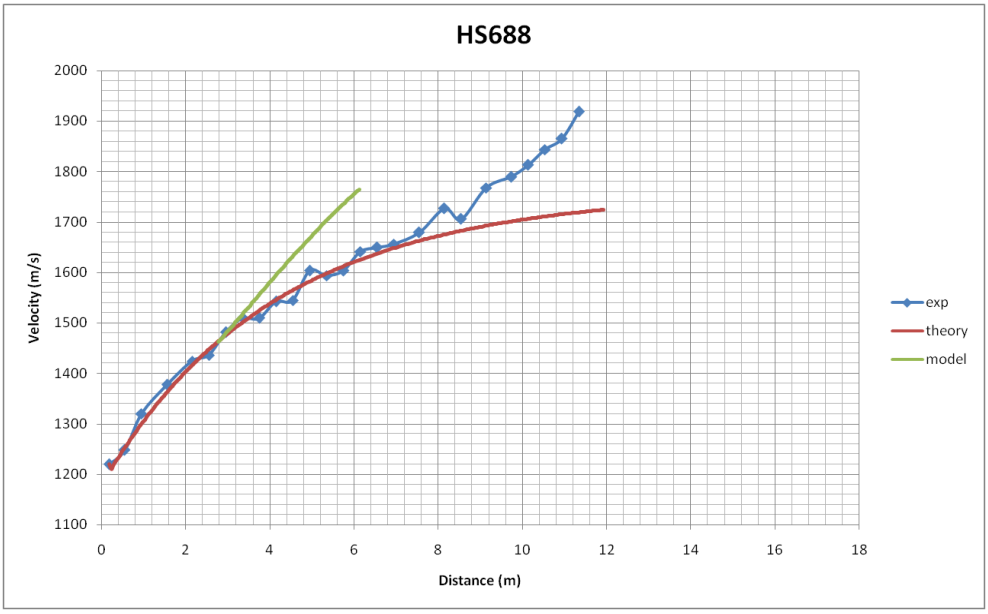

Fig. B.5 HS688, UW, Al-alloy, 67.25 g, 22 atm

Fig. B.6 HS689, UW, Mg-alloy, 66.38 g, 23 atm

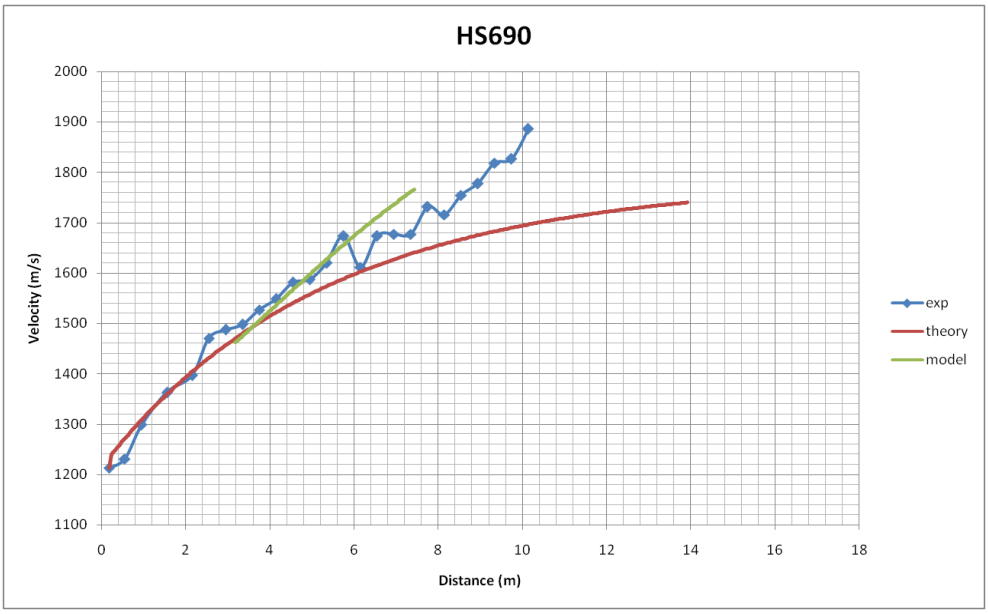

Fig. B.7 HS690, UW, Al-alloy, 85.2 g, 22 atm

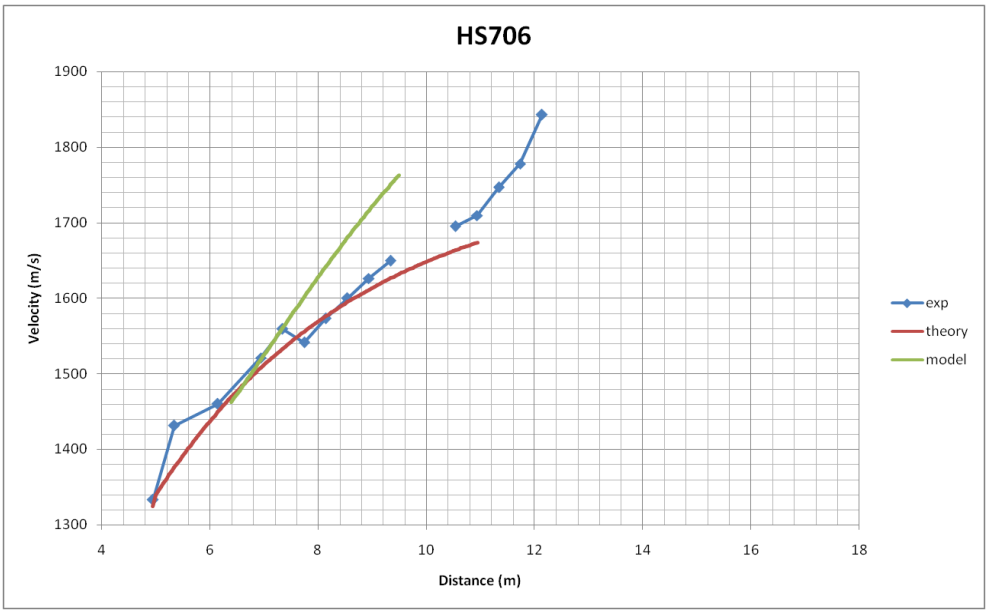

Fig. B.8 HS706, UW, Mg-alloy, 64.8 g, 22 atm

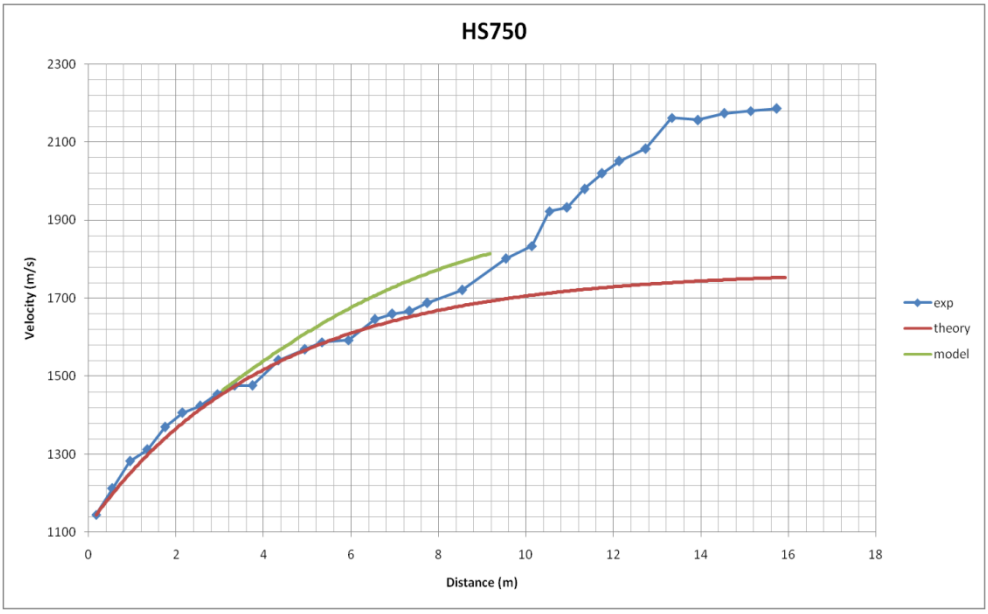

Fig. B.9 HS750, UW, Mg-alloy, 66.32 g, 20 atm

Fig. B.10 HS753, UW, Mg-alloy, 67.06 g, 21 atm

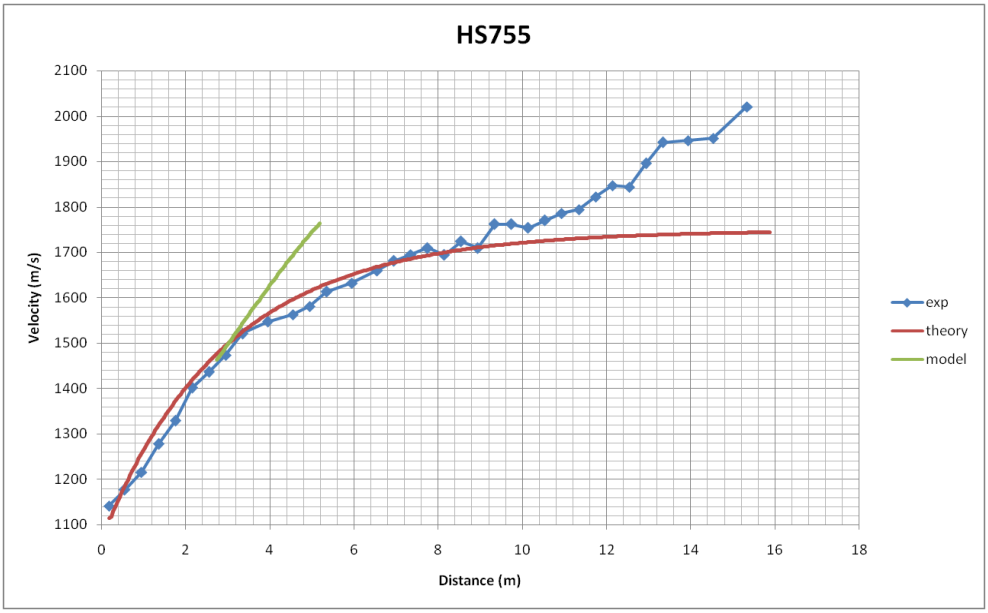

Fig. B.11 HS755, UW, Al-alloy, 77 g, 33 atm

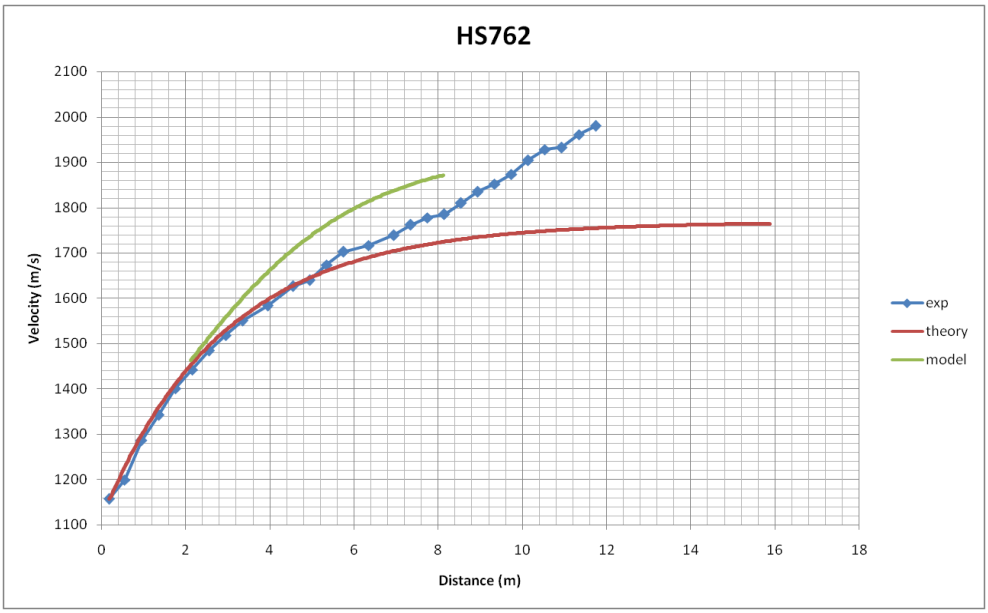

Fig. B.12 HS762, UW, Mg-alloy, 73.68 g, 33 atm

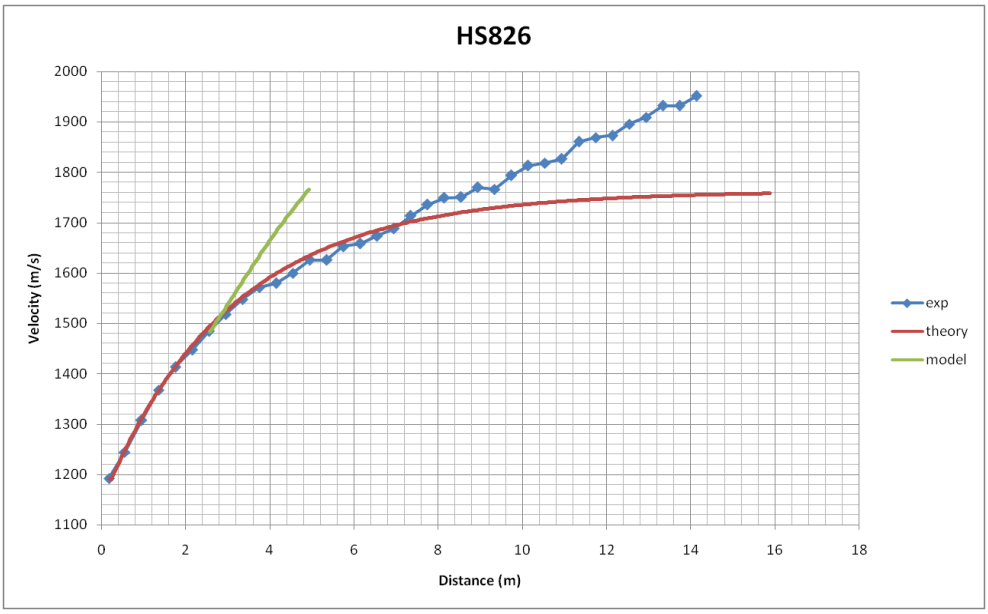

Fig. B.13 HS826, UW, Al-alloy, 72.4 g, 30 atm

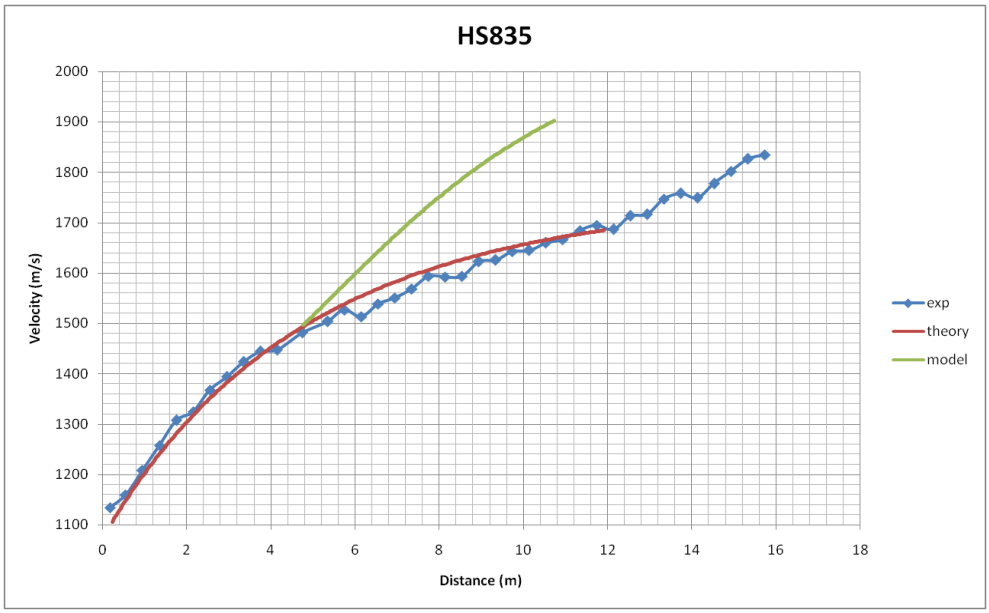

Fig. B.14 HS835, UW, Al-alloy, 88.4 g, 23 atm

Fig. B.15 HS843, UW, Mg-alloy, 64.11 g, 26 atm

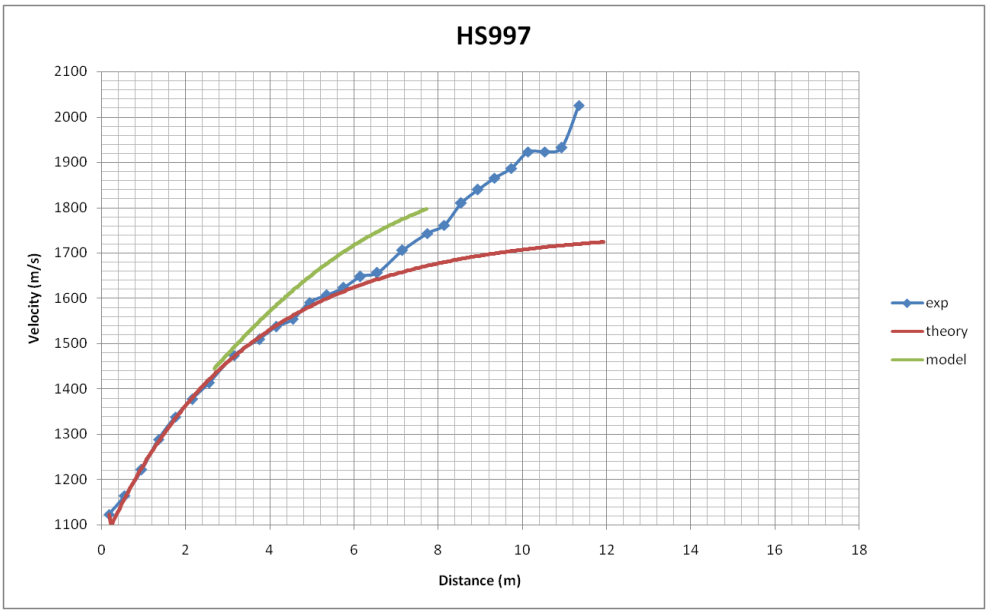

Fig. B.16 HS997, UW, Mg-alloy, 63.3 g, 23 atm

Fig. B.17 HS999, UW, Mg-alloy, 64.02 g, 24 atm

Fig. B.18 HS1000, UW, Mg-alloy, 63.72 g, 24 atm

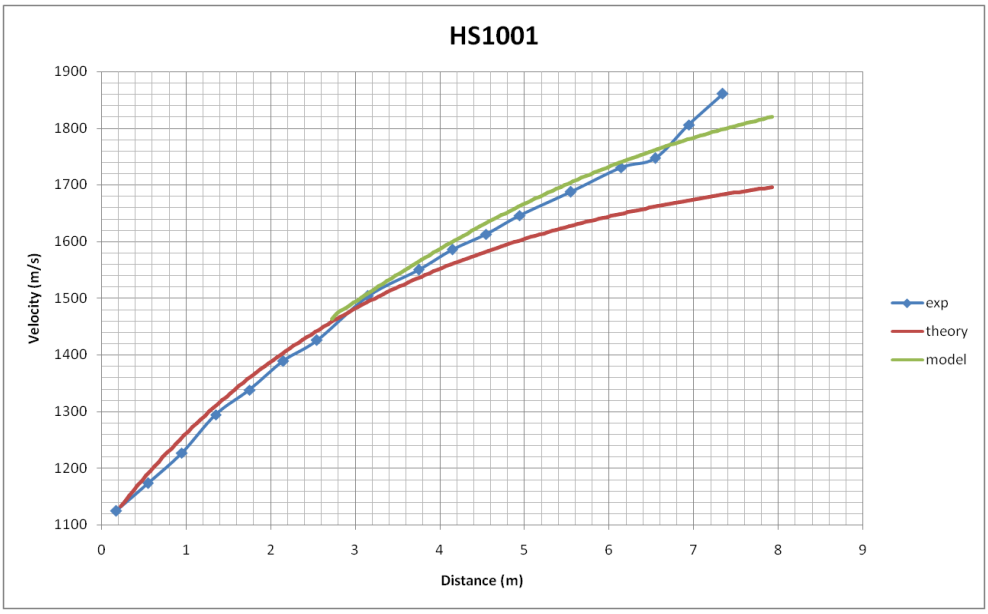

Fig. B.19 HS1001, UW, Mg-alloy, 63.44 g, 24 atm

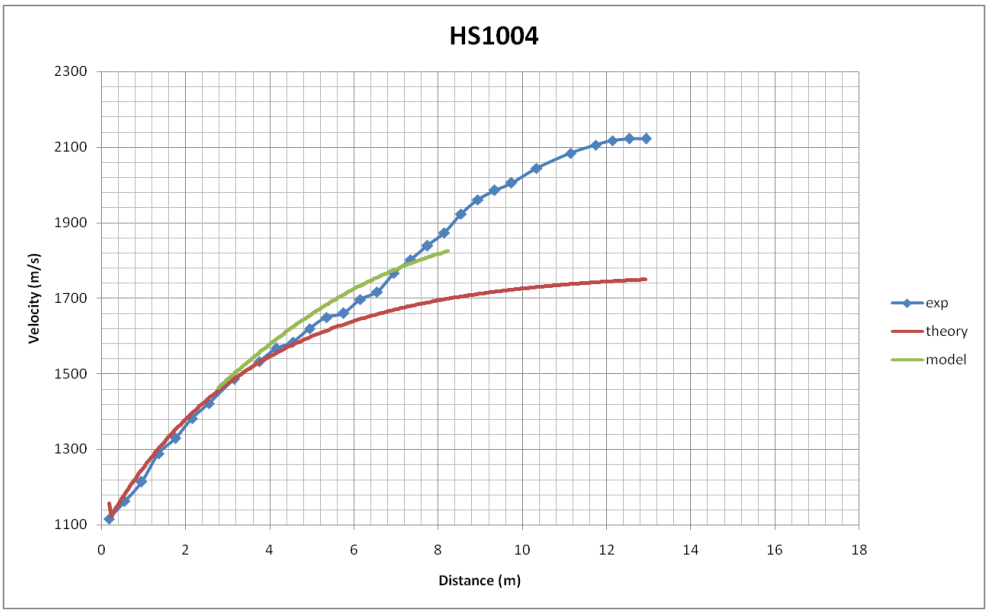

Fig. B.20 HS1004, UW, Mg-alloy, 64.31 g, 24 atm

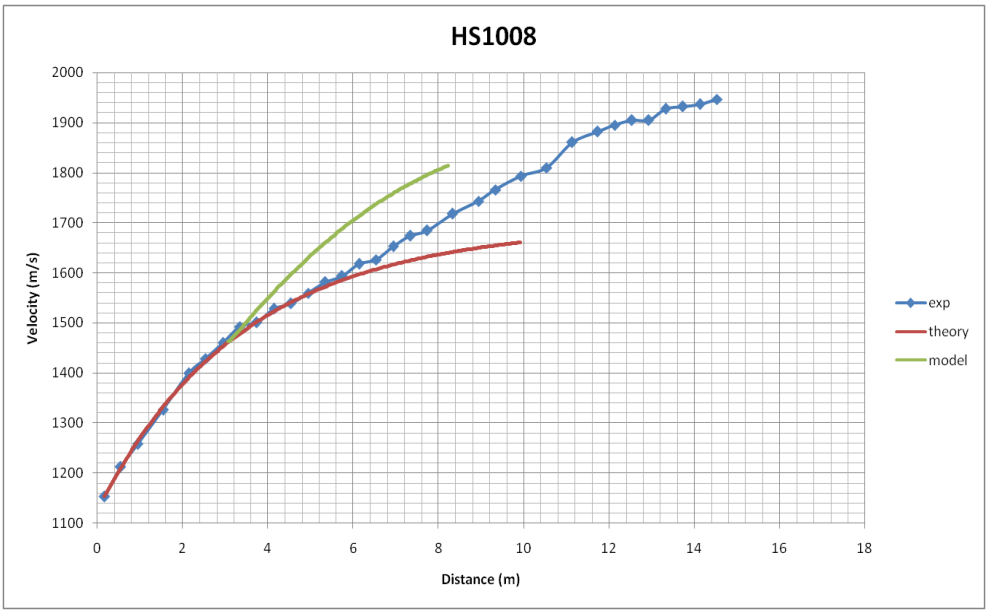

Fig. B.21 HS1008, UW, Mg-alloy, 64 g, 24 atm

Fig. B.22 HS1017, UW, Mg-alloy, 64.54 g, 24 atm

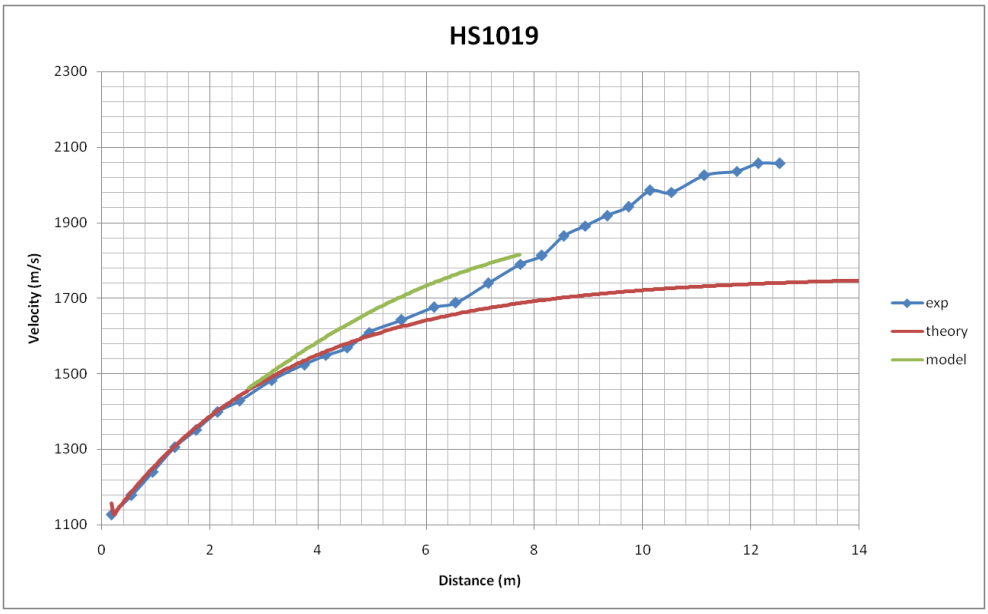

Fig. B.23 HS1019, UW, Mg-alloy, 62.29 g, 24 atm

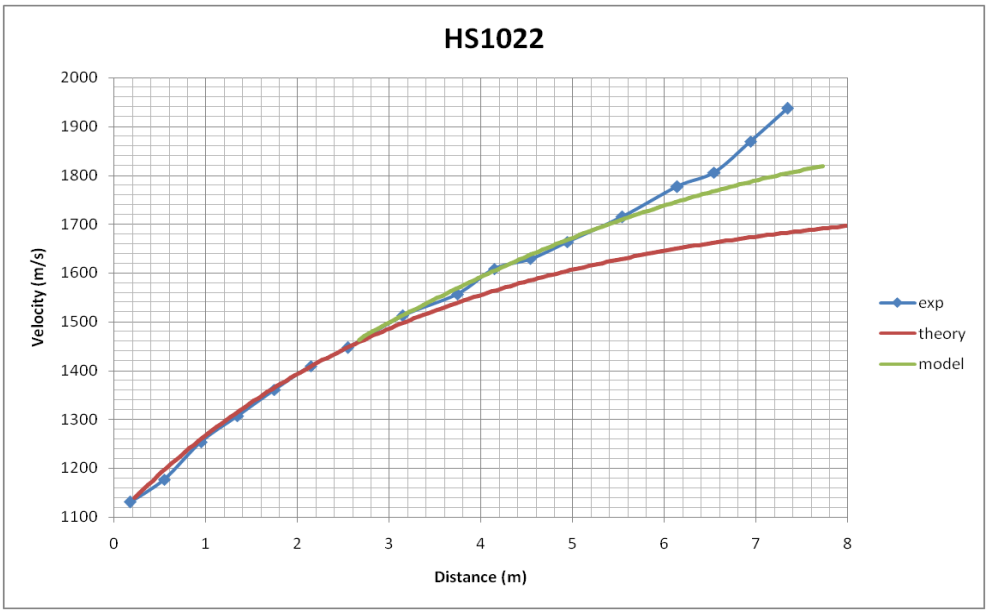

Fig. B.24 HS1022, UW, Mg-alloy, 62.76 g, 24 atm

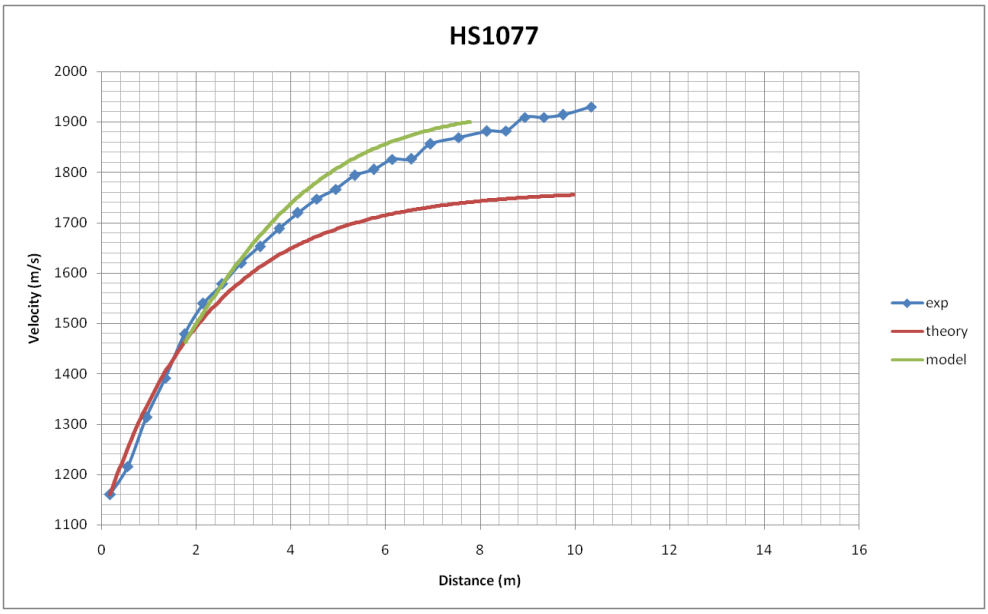

Fig. B.25 HS1077, UW, Al-alloy, 76.71 g, 30 atm

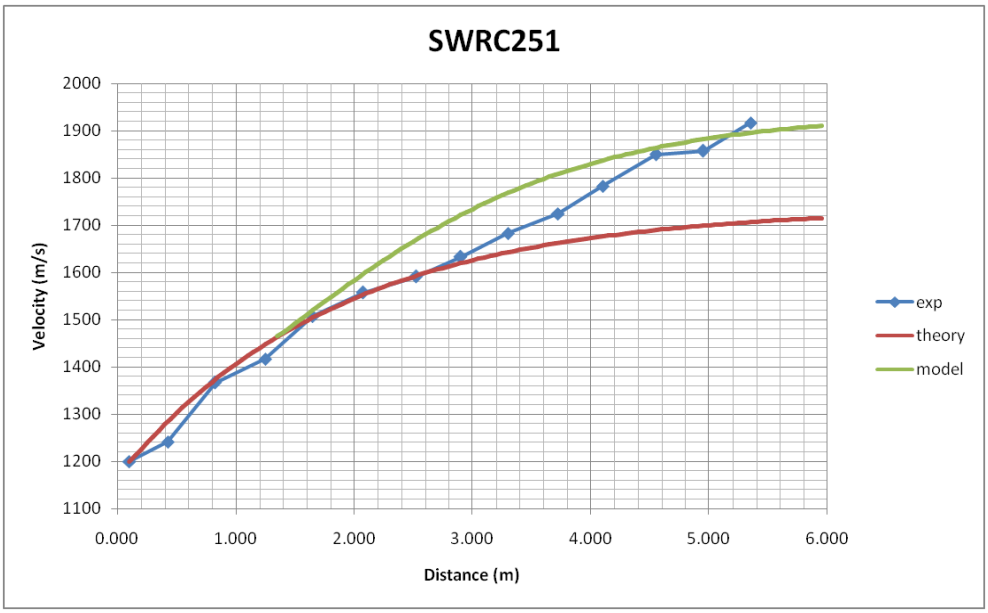

Fig. B.26 SWRC25 1st data set, SWR, Al-alloy, 22.5 g, 35 atm

Fig. B.27 SWRC25 2nd data set, SWR, Al-alloy, 22.5 g, 25 atm

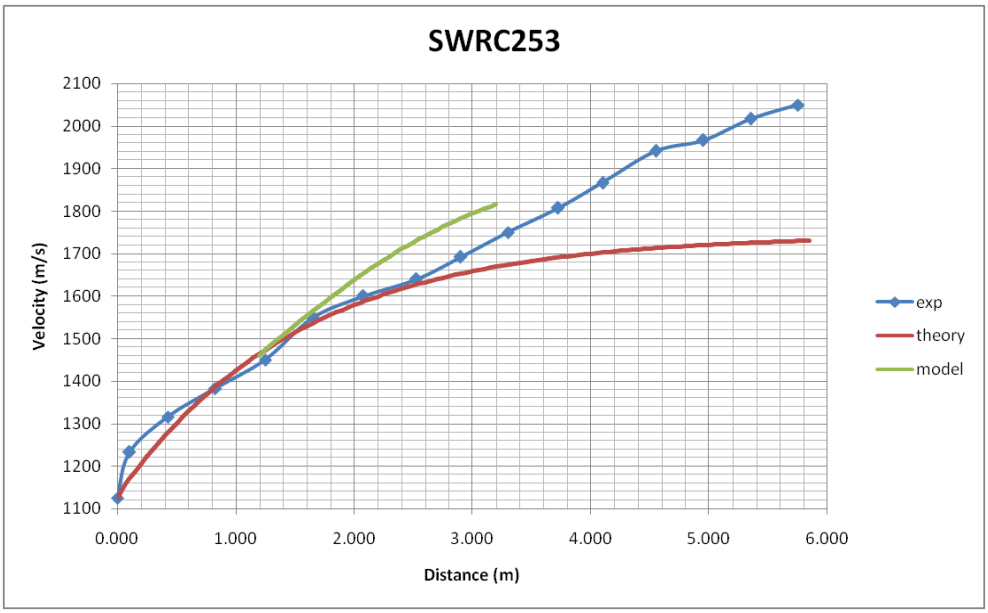

Fig. B.28 SWRC25 3rd data set, SWR, Al-alloy, 18.5 g, 35 atm

Fig. B.29 SWRC25 4th data set, SWR, Al-alloy, 18.5 g, 35 atm

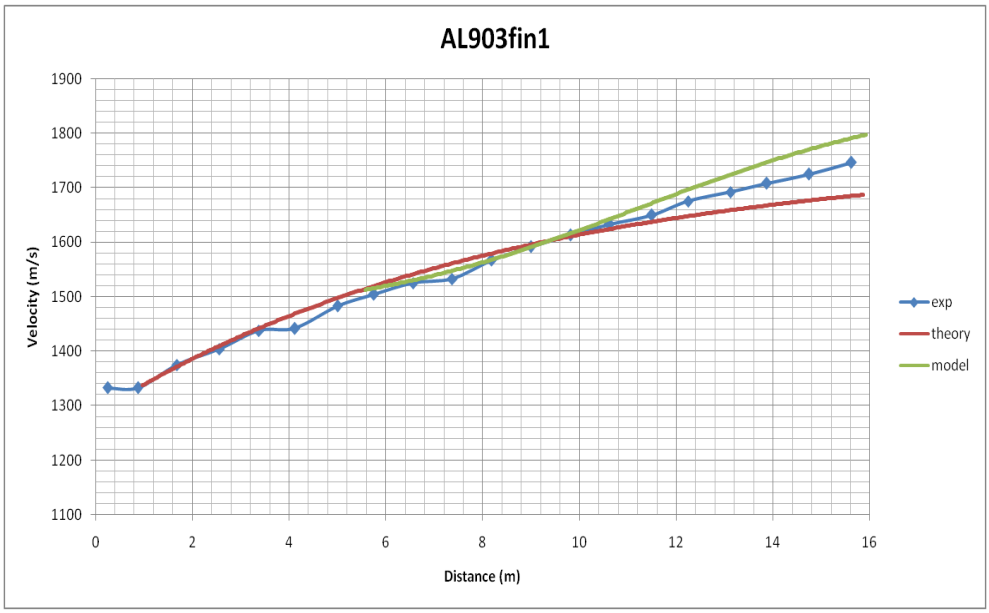

Fig. B.30 AL 90 3 fin 1st data set, ISL, Al-alloy, 1.3 kg, 40 atm

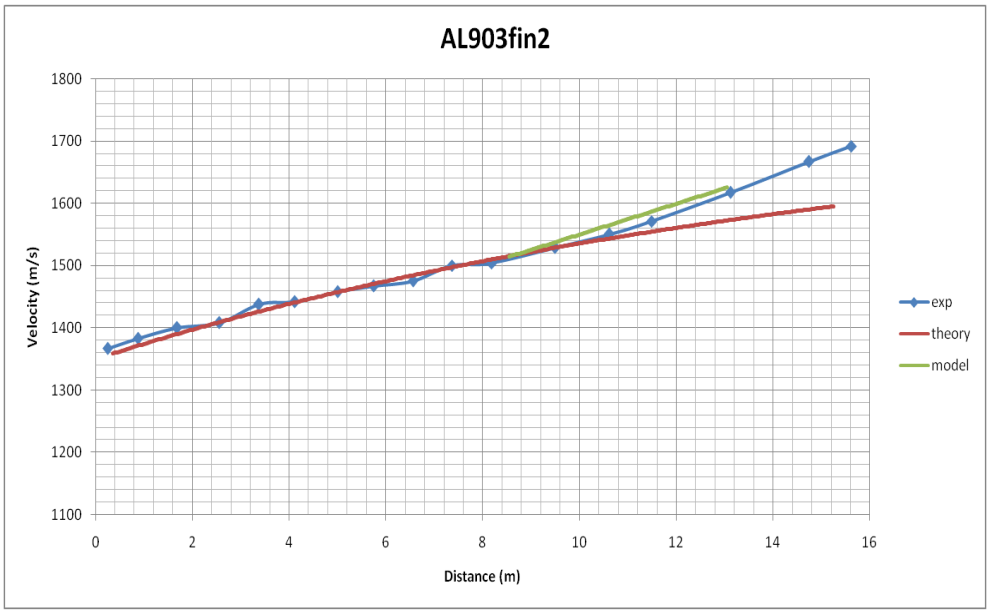

Fig. B.31 AL 90 3 fin 2nd data set, ISL, Al-alloy, 1.25 kg, 40 atm

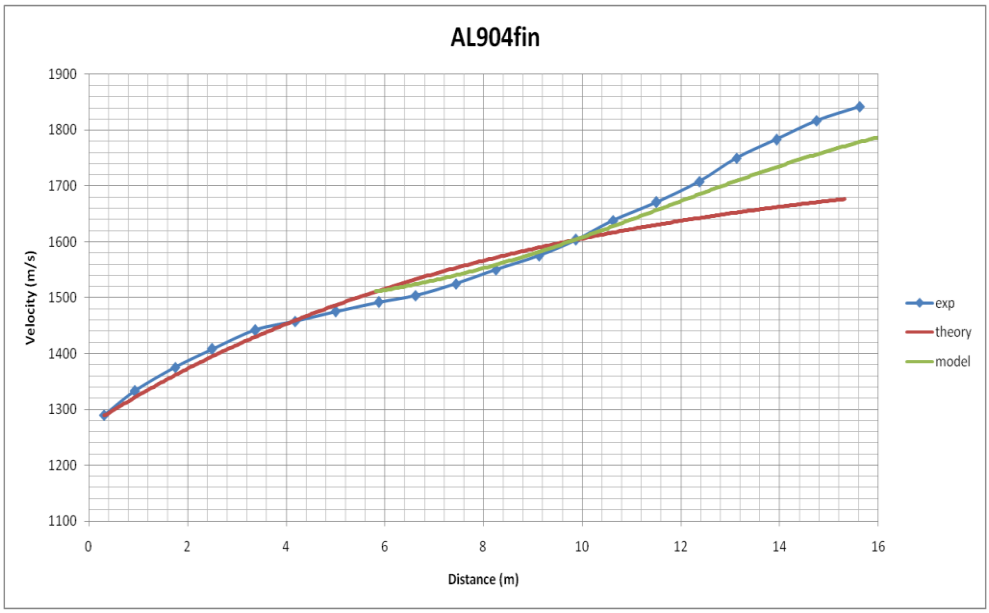

Fig. B.32 AL 90 4 fin, ISL, Al-alloy, 1.33 kg, 40 atm

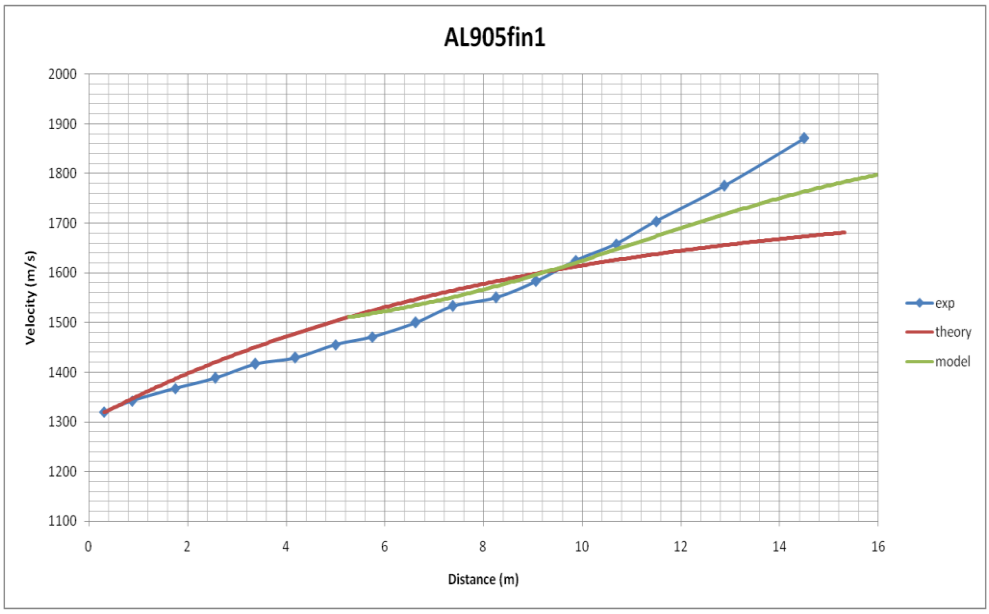

Fig. B.33 AL 90 5 fin 1st data set, ISL, Al-alloy, 1.33 kg, 40 atm

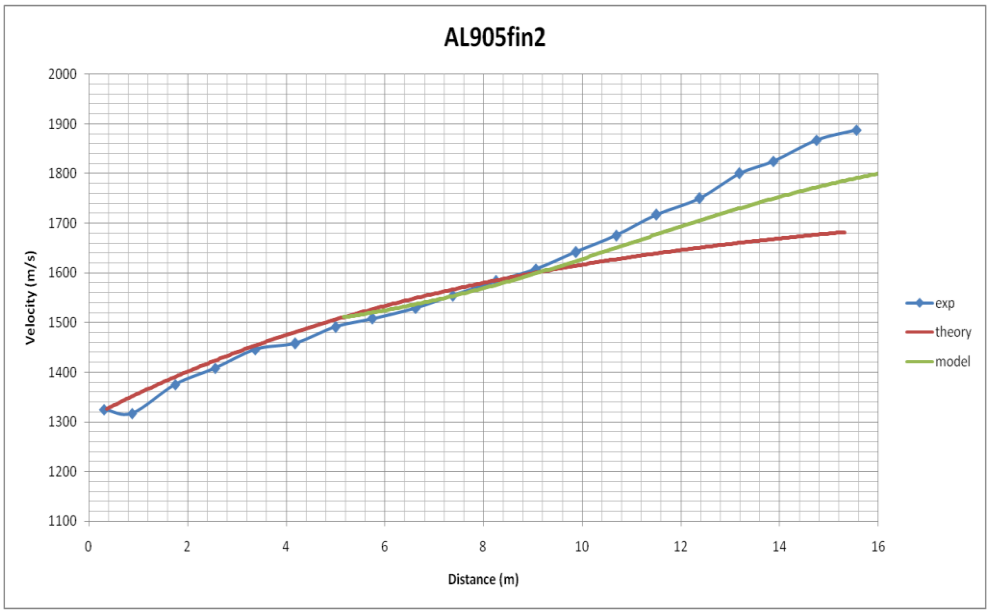

Fig. B.34 AL 90 3 fin 2nd data set, ISL, Al-alloy, 1.33 kg, 40 atm

References

1. *Ram Accelerator A New Chemical Method for Accelerating Projectiles to Ultrahigh Velocities.* **Hertzberg A., Bruckner A. and Bogdanoff D.** 1988, AIAA Journal Vol 26, No 2, pp. 195-203.

2. **Imrich T.** *The Impact of Projectile Geomtery on Ram Accelerator Performance.* Seattle : University of Washington, 1995.

3. **Kivity Y.** *Projectile Propelling System. 5303632* Israel, April 16, 1994.

4. **Knowlen C.** *Theoretical and Experimental Investigation of the Thermodynamics of the Thermally Choked Ram Accelerator.* Seattle : University of Washington, 1990. PhD dissertation.

5. *Experimental Investigation of Ram Accelerator Propulsive Modes.* **Hertzberg A, Bruckner A. and Knowlen C.** 1991, Vols. 1, page 17-25.

6. **Dunmire B.** *An Experimental and Theroretical Investigation of Single Stage Ram AcceleratorPerformance with Emphasis Towards Projectile Material Effects.* Seattle : University of Washington, 1991. MS Thesis.

7. *Heatind and Ablation of Projectile During Acceleration in a Ram Accelerator Tube.* **Naumann K.** Monterey, CA : AIAA, 1993. 93-2184.

8. **Chew G.** *Projectile Nose Heating in the Ram Accelerator.* Seattle : University of Washington, 1995. PhD Dissertation.

9. **Strehlow R.** *Combustion Fundamentals.* New York : McGraw-Hill, 1984. pp. 114-39, 302-36, 360-4.

10. **Shapiro A.** *The Dynamics and Thermodynamics of Compressible FLuid Flows.* New York : Ronald Press, 1953. pp. 73-262, 689-98, 1153-59.

11. **Wikipedia.** *wikipedia.org.* [Online] [Cited: November 10, 2015.] https://en.wikipedia.org/wiki/Ablation.

12. **Holman J.** *Heat Transfer.* s.l. : McGraw-Hill, 1963. pp. 622.

13. *Bow Shock Wave Heating and Ablation of a Sharp Nosed Projectile Flying at Superosonic Velocity inside of a Ram Accelerator.* **Seiler F. and Naumann K.** Marseille : 19th International Symposium on Shock Waves, 1993.

14. **ANSYS.** *Advanced Heat Transfer Topics.* [Document] s.l. : ANSYS customer training material, 2010.

15. *Operational Characteristics of the Thermally Choked Ram Accelerator.* **Bruckner A., Knowlen C., Hertzberg A. and Bogdanoff D.** 5, Seattle : Journal of Propulsion, Vol. 7.

16. *Unsteady Effects on Ram Accelerator Operation at Elevated Fill Pressures.* **Bundy C., Knowlen C. and Bruckner A.** 5, Seattle : Journal of Propulsion and Power, 2004, Vol. 20.

17. **Rathakrishnan E.** *Gas Dynamics.* Chapter: Normal Shock Waves : Prentice Hall, 2011. ISBN-10: 812034197X.

18. **Depraz S.** *New Tools for Ram Accelerator Performance Modeling.* Seattle : University of Washington, 2007.

19. *Modern Engineering for Design of Liquid Propellant Rocket Engines.* **Huang D., Huzel K. and David H.** s.l. : AIAA, Vol. 147.

20. **Pourpoint T.** engineering.purdue.edu/CEA%20Training. *engineering.purdue.edu.* [Online] [Cited: November 12, 2015.] https://www.google.com/search?site=&source=hp&q=nasa+cea+training+ppt&oq=nasa+cea+training+ppt&gs

_l=hp.3...1101.5114.0.5262.21.21.0.0.0.0.118.1630.16j4.20.0....0...1c.1.64.hp..1.14.1150...0j0i131j0i155i3j0i3j0i22i30j33i21.LkQoP6qBcH8.

21. **Bartz D.** *Advanced in Heat Transfer, Vol. 2.* New York : Academic Press, 1965. ISBN-10: 0120200023 .

22. *University of Washington High Pressure Ram Accelerator Facility.* **Knowlen C., Bundy C., Schwab R. and Bruckner A.** Pleasanton : 50th Meeting of the Aeroballistic Range Association, 1999.

23. **Chistofferson E.** *A Magnetic Transducer Detection System for High Speed Projectiles in Tubes.* Seattle : Univeristy of Washington, 1989. MS Thesis.

24. **Knowlen C.** ramaccelerator.org. [Online] University of Washington. [Cited: May 26, 2016.] ramaccelerator.org/home/node11.

25. *RAMAC in Subdetonative Propulsion Mode.* **Giraud M., Legendre J. and Henner M.** Saint-Louis, France : Third International Workshop on Ram Accelerators, 1997.

26. **Knowlen C.** ramaccelerator.org. [Online] University of Washington. [Cited: May 26, 2016.] ramaccelerator.org/otherfacilites.html.

27. *Kinetic Model for Aluminum-Sensitized Ram Accelerator Combustion.* **Catorie L., Legendre J., Giraud M.** 2, Saint-Louis : Journal of Propulsion and Power, 2003, Vol. 19.

28. *Recent Progress in RAMAC25 Operation.* **Hamate Y., Utsunomiya G., Sasoh A. and Takayama K.** Sendai, Japan : Fourth International Workshop on Ram Accelerators, 1999.

29. *High Ram Acceleration Using Open-Base Projectile.* **Yuichiro H., Akihiro S. and Kazuyoshi T.** 2, s.l. : Jounral of Propulsion & Power, 2003, Vol. 19.

30. *What about the Ram Accelerators? History, Principles, Performances and Applications.* **Giraud M., Burckner A., Takayama K., Bauer P., Knowlen C., Hamate Y.** Freiberg : 55th ARA Meeting, 2004.

31. **Glassman, I.** *Combustion.* Orlando : Academic Press, 1987. pp. 182-92, 198-226.

32. **Lifshitz, Landau L. and E.M.** *Fluid Mechanics.* Oxford : Pergamon Press, 1984. pp. 319-32, 337-41, 347-53, 480-96.

33. **Knowlen C.** ramaccelerator-home. *rameccelerator.org.* [Online] University of Washington. http://ramaccelerator.org/home/.